

THE UNIVERSITY
OF ADELAIDE
AUSTRALIA



High pressure metamorphism during intracratonic orogenesis: physical conditions and rates from the Amata region, Musgrave Province

Honours Thesis

Brianna Telenko

10/25/2010

Table of Contents

Abstract	3
1. Introduction.....	4
2. Geological setting	5
3. Metamorphic Petrology.....	8
3.1 Overview	8
3.1.1 Felsic mylonites	8
3.1.2 Dolerite Dykes	9
3.1.3 Mafic mylonites	9
3.1.4 Hornblende-bearing mylonites.....	10
3.1.5 Coronitic clinopyroxene-bearing mylonites	10
4. Methods.....	11
4.1 Mineral Chemistry	11
4.2 LA-ICP-MS U-Pb Monazite Geochronology	11
4.3 P-T estimations	12
4.4 Thermal modelling and garnet diffusion.....	13
5. Results.....	13
5.1 Mineral Chemistry	13
5.1.1 Garnet.....	13
5.1.2 Hornblende.....	14
5.1.3 Pyroxene.....	15
5.1.4 Feldspar	16
5.1.5 Fe- Ti oxides	16
5.1.6 Biotite.....	17
5.2 LA-ICPMS U-Pb Monazite Geochronology.....	17
5.2.1 Overview	17
5.2.2 Sample A325-875A.....	17
5.2.3 Sample A325-318.....	18
5.2.4 Sample A325-507A.....	18
5.2.5 Sample A325-917D.....	19
5.2.6 Sample A325-882.....	20
5.3 P-T estimates	20
5.3.1 Sample A325-535A.....	20
5.4 Thermal modelling and garnet diffusion.....	21
6. Discussion and conclusion	21
7. Acknowledgements	29
8. Appendices.....	30
9. References	37
10. Figure Captions.....	41
11. List of Tables	43
12. Tables	44
13. Figures	47

Abstract

The intracratonic orogenesis of the Petermann Orogeny caused the formation of high-pressure, low-geothermal gradient, eclogite facies rocks. These geologically rare rocks are found in the exposed orogenic core, observable near the Traditional community of Amata, in the Musgrave Province. Their formation remains a mystery and as a result two contrasting models have been proposed to explain their formation; namely whether orogenesis occurred in “hot” crust and was long lived, or occurred in “cold” crust and was short-lived. *In situ* LA-ICP-MS analysis of monazite show that metamorphism occurred at *c.* 598 Ma. Using conventional thermobarometric techniques, peak conditions are estimated to have reached ~640 °C and ~11.5 kbar. Integrating this data with petrological observations and calculated *P-T* pseudosections, a clock-wise *P-T* path was defined, which is typical of an orogenic setting. Diffusion modelling using garnet compositional profiles from grains of both relict composition and those interpreted to be reset, estimated the minimum duration for prograde metamorphism to be ~27 Myr. The same garnet grains show little to no evidence of cooling/exhumation, which has been attributed to the low metamorphic peak temperature. Results of this study make a direct contribution to two contrasting models for orogenesis. Combining new evidence from this study with tectonothermal evidence from the western Musgrave Province and sedimentological data from the Officer Basin to the south, it is concluded that shear heating (or short-lived deformation) is not a plausible model for Petermann-aged deformation. Despite the lack of spatially continuous data across the Musgrave Province, long-lived orogenesis is the more supported model in light of new evidence emerging from this study.

1. Introduction

High pressure metamorphism, particularly rocks of transitional eclogite and eclogite facies metamorphic conditions, are relatively rare in ancient geological record. Such rocks have typically been interpreted as indicative of tectonic plate margin type environments (amongst others; Schmidberger *et al.* 2007; Warren *et al.* 2008; Ravna *et al.* 2010). Apparently even rarer in the geological record are high-pressure, low-geothermal gradient metamorphic rocks that were produced as a result of intracratonic orogeny.

High pressure metamorphic rocks that formed in an intracontinental setting occur in the Musgrave Province in central Australia (Ellis & Maboko 1992; Camacho *et al.* 1997; Gregory *et al.* 2009). The Ediacaran-Cambrian aged Petermann Orogeny is a deeply exhumed intracontinental orogen that involved crustal shortening of >100km (Flöttmann *et al.* 2004), the production of large-scale, large-volume foreland basins in the current Amadeus and Officer basins (Wade *et al.* 2005) and produced one of the largest intracontinental gravity gradients on Earth (Korsch *et al.* 1998). Contractional orogenesis of the Petermann Orogeny occurred at *c.* 550Ma (Camacho *et al.* 1997) many hundreds of kilometres from any plate margin. The exposed orogenic core is of particular interest as it preserves sub-eclogitic to eclogitic (~12 kbar, ~650 °C) facies rocks (Camacho & McDougall 2000) in discrete, crustal-scale mylonitic shear zones. The eclogitic mineral assemblage has been dated at *c.* 550 Ma (Maboko *et al.* 1992; Camacho *et al.* 1997) and therefore it can be interpreted that the formation of these eclogites was synchronous with the intracratonic orogenesis at the time.

The duration of the Petermann-aged metamorphism and exhumation is variously estimated as ranging from approximately <1 Myr to >70 Myr (Lindsay & Leven 1996; Wade *et al.* 2005; Camacho *et al.* 2009). This estimation of the duration of metamorphism creates a paradox, as

long lived tectonism is not typically considered to comprise regionally cold, strong lithosphere conducive to the generation of low geothermal gradient rocks (Spear 1993). By contrast, short-lived tectonism, while being more conducive to a colder crustal thermal structure, has difficulty in accounting for the extreme amount of exhumation and generation of thick, foreland deposits with a protracted depositional history (Calver & Lindsay 1998; Wade *et al.* 2005).

A thorough understanding of the duration and evolution of the Petermann Orogeny and its significance in terms of the intraplate orogeny is hampered due to a paucity of time-integrated thermal and physical conditions. This study significantly contributes to understanding the evolution of the Petermann Orogeny by constraining the pressure-temperature-time evolution of high pressure rocks from the high-grade core of the orogen, located close to the Traditional community of Amata. This study is the first to use an approach integrating *in situ* geochronology with modern metamorphic analysis and diffusion-based thermal modelling estimations to understand the Petermann Orogeny. The findings of this study allow for an appraisal of the two contradicting models proposed for orogenesis; namely short-lived metamorphism accompanied by “cold” crust or long-lived metamorphism in “hot” crust, and further provide a framework with which to understand the intriguing nature of intracratonic orogeny.

2. Geological setting

The Musgrave Province is a Palaeo-Mesoproterozoic basement block that spans northern South Australia, southern Northern Territory and the east of Western Australia (Wade *et al.* 2008) (Fig.1). The basement province is surrounded by Neoproterozoic to Phanerozoic sedimentary basins, including the Canning, Amadeus and Officer Basins (Fig. 2) that have

been interpreted to be periodically contiguous (as the Centralian Superbasin) prior to the exhumation of the Musgrave Province. The Musgrave Province is cut by several E-W trending fault structures, which separate rocks that can be distinguished due to differing metamorphic grades and deformation structures (Maboko 1992). To the north, the Woodroffe Thrust separates amphibolite facies granitic gneisses of the footwall from granulites and high-pressure amphibolites of the hanging wall. The Davenport Shear Zone, which contains the documented near-eclogite facies mineral assemblages, separates these high-pressure granulites of the hanging wall. Despite being identified as being isotopically and metamorphically identical, the granulites to the south of the Davenport Shear Zone are noted to be more hydrated than their counterpart to the north of the shear zone. Camacho & Fanning (1995) suggest that whilst the subdomains, separated by these E-W trending fault zones, have previously been thought to have undergone different histories (Collerson 1972; Maboko *et al.* 1992), it is expected that differences are limited to only metamorphic grade, and hence these differences relate to their respective positions within the crust. Rocks to the south of the Mann Fault (Fig. 2) are seemingly little-affected by high-pressure, relatively pervasive, Petermann-aged deformation. These rocks comprise high-temperature granulite facies gneisses and mafic-ultramafic intrusions and volcanics of the long-lived Musgrave Orogeny, Mt West Orogeny, and Giles Event, respectively (Maboko *et al.* 1991; Evins *et al.* 2010; Smithies *et al.* 2010).

The earliest recorded event in the Musgrave Province was the emplacement of felsic gneiss of volcanic and granitic origin (*c.* 1600-1540 Ma), followed by upper amphibolite metamorphism at *c.* 1560 Ma, and an additional episode of felsic gneiss emplacement at *c.* 1324- 1296 Ma (Wade *et al.* 2008). Granulite facies metamorphic conditions were reached *c.* 1324- 1293 Ma, accompanied by migmatization of the orthogneiss (White *et al.* 1999; Smithies *et al.* 2010). A subsequent granulite facies event, the Musgrave Orogeny (*c.* 1230-

1150 Ma), reached conditions of ~6 kbar and ~850 °C (Camacho & Fanning 1995; Wade *et al.* 2008). This event was a regional metamorphic event, pervasively affecting the entire Musgrave Province. Synchronously, the emplacement Pitjantjatjara Supersuite (*c.* 1220- 1120 Ma) occurred. Following this, a series of magmatic events, starting with the emplacement the Giles Intrusions and associated volcano-sedimentary sequences (*c.* 1075 Ma), the Alcurra Dyke Swarm (*c.* 1080 Ma) and finally the Amata Dyke Swarm (*c.* 820 Ma) (Wade *et al.* 2008; Evins *et al.* 2010).

The final major event to affect the Musgrave Province was the ~620–530 Ma Petermann Orogeny (Camacho *et al.* 1997; Scrimgeour & Close 1999; Wade *et al.* 2005). The Petermann Orogeny was responsible for extreme basin inversion and deep exhumation of the Musgrave Province to the surface. Fragmentation of the once continuous Centralian Superbasin produced the smaller Amadeus and Officer basins preserved today (Walter *et al.* 1995). This intraplate orogenic event contributed to the construction and reactivation of the E-W trending fault architecture of the area (Hand & Sandiford 1999), including the Mann Fault, Woodroffe Thrust and the Davenport Shear Zone. The development of a basement-cored nappe (Flöttmann & Hand 1999; Aitken 2008) on the northern margin of the Musgrave Province accommodated extensive (>100 km) shortening during the Petermann Orogeny (Flöttmann *et al.* 2004). The Davenport Shear zone is a crustal-scale mylonitic and transpressional (Camacho *et al.* 2009) shear zone located between the Mann Fault and Woodroffe Thrust and represents the exposed core of the Petermann Orogen. Rocks from the Davenport Shear Zone preserves sub-eclogitic to eclogitic (~12 kbar, ~650 °C) facies mineral assemblages (Camacho & McDougall 2000) and has been dated at *c.* 550 Ma (Ellis & Maboko 1992; Camacho *et al.* 1997).

3. Metamorphic Petrology

3.1 Overview

The predominant metamorphic facies from the Amata region, adjacent to the Davenport Shear Zone, is granulite facies rocks, formed during the 1230- 1150 Ma (Wade *et al.* 2008) Musgrave Orogeny. However, the Davenport Shear Zone, and associated mylonites contain eclogitic to sub-eclogitic facies rocks that formed during the Petermann Orogeny (Maboko *et al.* 1992; Camacho *et al.* 1997). Evidence for this high-pressure event can also be seen in the surrounding granulite facies rocks by the presence of minerals such as kyanite and metamorphic reaction textures that overprint the granulite facies assemblages.

A compilation of approximately sixty samples have been examined from a series collected by Collerson (1972) as part of a PhD study. These samples have been collected from various locations within the Amata region. Figure 3 shows the spatial distribution and field relationships of these samples. They have been placed into five major groups, which are discussed below, and the key petrological features of each are shown in Fig. 4. Appendix A lists each sample in the study along with its petrological group, lithology (according to Fig. 3) and the data collected.

3.1.1 Felsic mylonites

Felsic mylonites have a garnet-plagioclase-K-feldspar-quartz-ilmenite \pm magnetite mineralogy. The peak mineral assemblage is garnet-quartz-ilmenite. The garnet grains exist as two distinct microstructural types; either as large (0.25-4 mm) porphyroclasts or as fine grained coronas around ilmenite and plagioclase grains. The garnet porphyroclasts have been wrapped by the foliation which is defined by mineral elongation (of ilmenite) and fine grained quartz aggregates (Fig. 4, A & B). These garnet grains range from rounded euhedral in shape to anhedral and in some cases form aggregates of anhedral garnet grains. Some garnet porphyroclasts are mantled by the finer grained garnet grains. Plagioclase occurs as

larger grains than quartz and often contains distinctive multiple twinning. Quartz occurs as either an aggregate of fine grains or as a ribbon habit. Monazite and zircon are common accessory minerals. Monazite (5 – 200 μm) often occurs as inclusions within garnet porphyroclasts or in direct contact with ilmenite and rutile in the matrix. Zircon is found also within garnet porphyroclasts but more rarely than monazite grains. More often it occurs at grain boundaries of plagioclase grains.

3.1.2 Dolerite Dykes

These are extremely fine-grained mafic rocks composed almost entirely of garnet and clinopyroxene (~90 %) with smaller proportions of plagioclase, ilmenite, quartz, \pm rutile \pm titanate \pm biotite. The rock is very fine grained and shows no reaction textures. The garnet and clinopyroxene grains exist as anhedral porphyroclasts of 0.25-1mm as well as smaller anhedral interlocking grains (Fig. 4, C & D). The smaller garnet grains are ovoid in shape and are aligned to define a foliation. The smaller clinopyroxene grains are equant and as a result do not define the foliation. Ilmenite grains occur as small rounded grains that also occur as aggregates. They have a random distribution, however ilmenite-rich darker bands alternating with paler ilmenite-poor bands, contribute to the foliation. Biotite, when observed, occurs as equant anhedral grains in the strain shadows of garnet porphyroclasts, as well as other sizeable ($>0.1\text{mm}$) grains.

3.1.3 Mafic mylonites

Mafic mylonites are well foliated and comprise mainly orthopyroxene, clinopyroxene, plagioclase, garnet, ilmenite, quartz and kyanite. Some samples also contain biotite, rutile and K-feldspar. The peak mineral assemblage is garnet-plagioclase-kyanite-quartz-ilmenite. The defining feature of these rocks is the relict pyroxenes (Fig. 4, E & D). Both clinopyroxene and orthopyroxene exist as relict grains. They are large grains (0.25- 1 mm) and often are in direct contact with ilmenite at their grain boundary. Garnet only occurs as very fine grains

surrounding ilmenite. Plagioclase (0.25 – 0.5mm) is anhedral and commonly contains inclusions of fibrous-acicular kyanite. Kyanite also occurs at plagioclase and pyroxene grain boundaries. The abundance of kyanite is variable from sample to sample. Quartz appears as fine grained aggregates or ribbons. The foliation is defined by quartz ribbons or strings of quartz aggregates, and elongated oxides.

3.1.4 Hornblende-bearing mylonites

The defining feature of this group is the presence of hornblende. The mineralogy consists of hornblende, plagioclase, garnet, clinopyroxene, orthopyroxene, ilmenite, biotite ± kyanite ± rutile ± titanite. The peak mineral assemblage, visible in the medium grained rocks, is hornblende-garnet-kyanite-ilmenite-rutile. The very fine grained rocks show no mineral reaction textures so no peak mineral assemblage can be determined. The medium grained rocks contain much coarser grained (1-4 mm) hornblende. Quartz grains (0.1 – 0.25 mm) are angular and blocky. The garnet exists only as fine grained aggregates, usually in contact with hornblende at the grain boundary (Fig. 4, F & G). Biotite is acicular and commonly occurs surrounding hornblende. Plagioclase grains are bladed to equant and are very large (1-4mm) and exhibit trade-mark multiple twins.

3.1.5 Coronitic clinopyroxene-bearing mylonites

These mylonites are characterised by clinopyroxene mantling relict orthopyroxene grains. They have a mineralogy of orthopyroxene, clinopyroxene, garnet, plagioclase, quartz, kyanite ± biotite. The peak mineral assemblage is clinopyroxene-garnet-kyanite-ilmenite-rutile-quartz. Orthopyroxene and the clinopyroxene grains occur as coarse porphyroclasts but in addition, the clinopyroxene is also present as a corona around the relict orthopyroxene (Fig. 4, H & I). Garnet grains are fine grained and commonly occur mantling ilmenite. Kyanite mantles coronitic clinopyroxene and also occurs as fine-grained fibrous-acicular inclusions within plagioclase. Quartz grains vary in size from fine grained to medium grained. The

strong foliation present is due to mineral alignment (i.e. fine grained garnet trails) and mineral elongation (i.e. ilmenite and rutile). The coronitic clinopyroxene extends along the foliation.

4. Methods

4.1 Mineral Chemistry

Mineral chemical analyses were obtained using a Cameca SX51 electron microprobe at Adelaide Microscopy at the University of Adelaide, using a beam current of 20 nA and an accelerating voltage of 15 kV. Representative mineral analyses of all samples are presented in Appendix B. These have been recalculated to incorporate ferric iron using stoichiometric criteria (Droop 1987). Furthermore, elemental maps were obtained from domains of selected samples to characterise the 2D distribution of elements such as iron, calcium, magnesium and manganese in possible zoned minerals like garnet. This was also undertaken using the Cameca SX51 using beam conditions of 110 nA and 15 kV.

4.2 LA-ICP-MS U-Pb Monazite Geochronology

In situ monazite geochronology was performed on polished thin sections. Prior to isotopic analysis, the microstructural location of monazite in thin section was determined using backscattered electron imaging on a Philips XL30 FEGSEM at Adelaide Microscopy. Monazite U-Pb geochronology was undertaken using a New Wave Nd-YAG laser (213 nm) coupled with an Agilent 7500cs ICPMS, following the procedures of Payne *et al* (2008). Ablation was conducted in a helium atmosphere with a beam diameter of 8 μm and a frequency of 5 Hz. The total acquisition time was 100 seconds, divided into 50 seconds of measuring background, 10 seconds for beam stabilisation and 40 seconds for sample ablation. Data reduction was conducted using GLITTER software (Van Achtebergh *et al.* 2001). The accuracy of the data produced was monitored using the internal standards MAdel (weighted

average of 527.7 ± 3.2 Ma) and Bruna-NW/ 222 (weighted average mean of 456.3 ± 2.3 Ma). Isoplot 4.11 was used to calculate final ages and construct concordia. Mass bias and fractionation were corrected for using the monazite standard 44069 as an external standard (Aleinikoff *et al.* 2006). Monazite data, shown as concordia plots and weighted average plots, are shown in Figs. 9- 13. All data collected from the LA-ICP-MS and processed in 'Glitter' is represented in Table 1. Ages quoted in this study that are >1000 Ma refer to $^{207}\text{Pb}/^{206}\text{Pb}$ ages and those <1000 Ma are $^{206}\text{Pb}/^{238}\text{U}$ ages.

4.3 P-T estimations

The aim in defining P - T conditions and paths is to give insight on the thermal conditions and evolution of the orogen. The bulk composition required for phase equilibria modelling for sample A325-535A was determined through solution ICPMS and the $\text{Fe}^{2+}/\text{Fe}^{3+}$ ratio was determined by titration at Amdel Laboratories, Adelaide. The P - T pseudosection was calculated using THERMOCALC v3.33 (update of Powell & Holland 1988), using the internally consistent data set of Holland & Powell (1998; data set tcds55, November 2003 update). The pressure-temperature pseudosection was calculated using the geologically realistic system NCFMASHTO (Na_2O - CaO - FeO - MgO - Al_2O_3 - SiO_2 - H_2O - TiO_2 - Fe_2O_3). The modelling for this system uses a - x relationships of White *et al.* (2007) for garnet, White *et al.* (2000) for ilmenite, White *et al.* (2002) for magnetite, Holland and Powell (2003) for plagioclase, Diener *et al.* (2007) for amphibole and Green *et al.* (2007) for clinopyroxene. The absolute values of compositional isopleths, as well as the trends in changing mineral composition in P - T space, can be used, in conjunction with measured mineral chemistry, to constrain P - T conditions and P - T path trajectory (Stüwe & Powell 1995; White *et al.* 2002; Kelsey *et al.* 2003a; Kelsey *et al.* 2003b).

P - T estimates were also obtained using the average P , average T and average PT functions available in THERMOCALC v3.33 (Powell & Holland 1988) and inputting measured

mineral compositions. Conventional thermobarometry is based on a set of independent end-member reactions relevant to the mineral phases chosen for calculations. The use of this conventional thermobarometric tool was to further constrain the sample within P - T space on the constructed pseudosection. In the case of sample A325-535A, thermobarometry provided a further constraint on the conditions of the sample. If a statistically allowable solution is not derived, the user may alter the system by omitting a mineral end-member or altering the P - T boundaries set (e.g. Powell & Holland 1994).

4.4 Thermal modelling and garnet diffusion

Transects of mineral chemistry were collected across garnet grains in sample A325- 907E.

Figure 5 shows the location of the transects for the sample. Each transect was analysed for a range of elements, with particular interest in iron, magnesium, manganese and calcium. Each transect bisects through a garnet-plagioclase pair, and compositional data was acquired with a spacing of between 5-15 μm between analysis spot locations. The Fe-Ca zoning patterns were utilised using the diffusion modelling code of Robl *et al.* (2007). An X_{Fe} ($X_{\text{Fe}} = \text{Fe}/(\text{Fe}+\text{Ca})$) and a X_{Ca} ($X_{\text{Ca}} = \text{Ca}/(\text{Ca}+\text{Fe})$) profile for each transect was created and used for the diffusion modelling. A range of parameters were set (see Table 2 for a full list for each transect) to produce models for the data. User defined T/t histories were applied to produce a better fit for the model. Freer and Edwards (1999) defined diffusion coefficients for Ca (Fe-Mg) diffusion using almandine-grossular diffusion couple experiment. However, the diffusion values for Fe were taken from Ganguly *et al.* (1998).

5. Results

5.1 Mineral Chemistry

5.1.1 Garnet

The garnet chemistry has been separated into “old” garnet (porphyroclastic garnets) and “new” garnet (garnet coronas and fine grained aggregates) (Table 3). The new garnet in the

felsic mylonites and hornblende-bearing mylonites tend to be dominated by an almandine-grossular solid solution. The felsic mylonites have average X_{alm} ($X_{alm} = Fe / (Fe + Mg + Ca + Mn)$) and X_{grs} ($X_{grs} = Ca / (Ca + Mg + Fe + Mn)$) values of 0.46 and 0.33, respectively and the hb-bearing mylonites have average X_{alm} and X_{grs} values of 0.57 and 0.25, respectively. The dolerites and coronitic clinopyroxene-bearing mylonites and mafic mylonites have much more significant average X_{py} ($X_{py} = Mg / (Mg + Ca + Fe + Mn)$) values (0.24 and 0.22, respectively) but are still marginally almandine-grossular dominated. The mafic mylonites have the highest X_{alm} value ($X_{alm} = 0.631$) but is still almandine-grossular dominated. The grain size of the “new” garnet growth is too small to resolve any zoning patterns from the analyses.

The felsic mylonites and hornblende-bearing mylonites have analyses of “old” garnet growth as well. Whereas garnet grains in the hornblende-bearing mylonites show no significant differences in end-member proportions between the two stages of growth, “old” garnet grains in the felsic mylonites show a marked decrease in the average X_{grs} value ($X_{grs} = 0.07$) and a subsequent increase in average X_{alm} ($X_{alm} = 0.52$) and average X_{py} ($X_{py} = 0.39$). Zoning patterns are visible in all “old” garnet growth from both groups, although the profiles are very shallow, with only a slight inflection at the rims. The patterns for each are the same with X_{grs} increasing from core to rim, X_{py} and X_{alm} decreasing from core to rim and X_{spss} ($X_{spss} = Mn / (Mn + Ca + Mg + Fe)$) showing no change from core to rim. See Fig. 6 for profiles for each garnet transect.

5.1.2 Hornblende

The majority of the analysed hornblende analyses are classified within the calcic amphibole group ($Ca_B + Na_B > 1.00$ and $Na_B < 0.50$), with a minority falling within the Mg-Fe-Mn-Li group ($Ca_B + Na_B < 1.00$ and $(Mg + Fe + Mn + Li)_B > 1.00$). Na_B and Ca_B refer to the occupation of the cations per the unit formula for amphiboles, $AB_2^{VI}C_5^{IV}T_8O_{22}$ (Leake *et al.* 1997). The

calcic amphiboles have an average X_{Fe} ($X_{Fe}=Fe^{2+}/Ti+Al+Fe^{2+}+Mg$) of 0.38 and an X_{Mg} ($X_{Mg}=Mg/Ti+Al+Fe^{2+}+Mg$) of 0.62 whilst the Mg-Fe-Mn-Li amphiboles have an average X_{Fe} of 0.59 and an average X_{Mg} of 0.41. The average values for all hornblende analyses in the hornblende-bearing mylonites (as shown in Table 3) more closely resemble those of the calcic group. This reflects the actuality that the calcic amphiboles are more voluminous with the samples.

5.1.3 Pyroxene

All pyroxene analyses have been classified using the system of Morimoto (1988). Figure 7 shows a plot of all pyroxene analyses on a Q-J diagram (where $Q = Ca + Mg + Fe^{2+}$ and $J = 2x Na$). The majority of the analyses plot within the Ca-Mg-Fe quadrilateral with few extending into the Ca-Na pyroxene group and “other” pyroxene group (Morimoto & Kitamura 1983).

Clinopyroxene chemistry has been subdivided into “old” and “new” growth, analogous to the garnet classification. All the “old” clinopyroxene analyses are further classified as diopside, with average X_{Ca} ($X_{Ca}=Ca/Ca+Fe^{3+}+Fe^{2+}+Mg+Mn$) values of 0.45-0.46. This is also the case for the “new” cpx growth for the dolerites and hornblende-bearing mylonites, where the clinopyroxene occurs as fine grained single grains within the matrix. However, in the coronitic clinopyroxene-bearing mylonites, the average X_{Ca} levels are slightly lower (average $X_{Ca} = 0.42$) and as a result are classified as augite. The X_{Na} ($X_{Na}=Na/(Na+Ca)$) varies only slightly (up to 17%) between “new” and “old” growth. Both the hornblende-bearing mylonites and coronitic clinopyroxene-bearing mylonites show a decrease in X_{Na} from “old” to “new” growth, whereas the dolerite dykes show an opposing trend.

The orthopyroxene analyses of both the coronitic clinopyroxene-bearing mylonites as well as mafic mylonites have uniformly average X_{Mg} ($X_{Mg} = Mg/Mg+Fe^{3+}+Fe^{2+}+Ca+Mn$) of approximately 0.50. The coronitic clinopyroxene-bearing mylonites and the mafic mylonite

differ primarily in their average X_{Fe} ($X_{Fe} = Fe/Mg+Fe^{3+}+Fe^{2+}Ca+Mn$ and $Fe = Fe^{3+} + Fe^{2+} + Ca$) values, which are 0.30 and 0.48, respectively.

5.1.4 Feldspar

Plagioclase in each sample is sodic, with the average X_{Na} values ranging from 0.54 to 0.93.

The lowest average X_{Ca} ($X_{Ca}=Ca/Ca+Na$) value is for the hornblende- bearing mylonites ($X_{Ca} = 0.069$) whilst the highest is for the mafic mylonites ($X_{Ca} = 0.438$). The orthoclase content is very low, with the maximum average X_K being 0.067.

Alkali feldspar is uniformly potassium rich with the average X_K values ranging from 0.75 to 0.92. The anorthite contents of alkali feldspar in the felsic mylonites and mafic mylonites are extremely low with the average X_{Ca} values being 0.061 and 0.005, respectively.

5.1.5 Fe- Ti oxides

The Mn content of the ilmenite in the felsic mylonites, hornblende- bearing mylonites and coronitic clinopyroxene- bearing mylonites are similar, with average X_{Mn} ($X_{Mn} = Mn/ Mn+ Fe+ Mg$) values of 0.003 to 0.004. The mafic mylonites have a slightly higher average X_{Mn} value of 0.011. The felsic mylonites and new cpx-bearing mylonites are all a haematite-ilmenite solid solution, with average X_{Ilm} ($X_{Ilm} = Ti/ Ti+ (1/2Fe^{3+})$) values of 0.73 and 0.65, respectively. The hornblende-bearing mylonites and mafic mylonites are much more haematite poor with average X_{Ilm} values of 0.99 and 0.92, respectively.

The presence of magnetite has only been detected in the coronitic clinopyroxene-bearing mylonites and the mafic mylonites. The chemistry is very similar for both groups with the X_{Al} ($X_{Al} = Al/(Al+ Fe^{3+} + 2Ti)$) for the coronitic clinopyroxene-bearing mylonites and mafic mylonites being 0.007 and 0.005, respectively. The TiO_2 wt % is 0.087 and 0.084, respectively.

5.1.6 Biotite

The iron levels of biotite are relatively similar across all samples, with the average X_{Fe} ($X_{\text{Fe}} = \text{Fe}/(\text{Fe} + \text{Mg})$) ranging from 0.27 to 0.34. The coronitic clinopyroxene-bearing mylonites have the lowest TiO_2 (wt %) of 3.7, in comparison to the dolerite dykes and mafic mylonites, whose values are 5.5 and 4.2 respectively.

5.2 LA-ICPMS U-Pb Monazite Geochronology

5.2.1 Overview

The primary aim of the geochronology was to constrain the age of deformation and metamorphism within the Davenport Shear Zone. Laser Ablation – Inductively Coupled Mass Spectrometry (LA-ICPMS) analysis was conducted on samples A325-875A, A325-318, A325-507A, A325-917D and A325-882. These samples were chosen as they provide mineralogical evidence of deformation during the interpreted Petermann Orogeny. Monazite grains were targeted that are contained within the mylonitic fabric and also within porphyroclastic minerals (garnet and pyroxene) that are interpreted to predate the formation of the mylonitic fabric.

5.2.2 Sample A325-875A

Thirty-seven analyses were conducted on thirty-five monazite grains from sample A325-875A (Fig. 8a). The targeted monazites were present in the mylonitic fabric. Of the thirty-seven analyses, only sixteen returned reliable signals. This was due to firing through the grain when ablating, or ablating too close to an edge or crack in a grain resulting in common lead contamination. This data was discarded and was not used in any further analysis. In order to account for any common lead incorporated into monazite, a Tera-Wasserburg Concordia plot, anchored to common lead (4550 Ma; Tatsumoto *et al.* 1973) was generated (Fig. 9a). A lower concordia intercept of 594 ± 50 Ma, with a MSWD of 0.64, resulted. The weighted average $^{206}\text{Pb}/^{238}\text{U}$ age of 598.8 ± 5.2 Ma ($n=16$) (MSWD of 0.61) is calculated for this sample (Fig. 9b).

5.2.3 Sample A325-318

Eighteen analyses were conducted on ten monazite grains from sample A325-318 (Fig. 8b). The targeted monazite grains occur within garnet grains and in the matrix in direct contact with ilmenite. All data is plotted on a conventional concordia in Fig. 10a. The analyses were separated into those taken from monazites inside garnet grains and those in contact with ilmenite in the matrix. The matrix analyses are represented on a Tera-Wasserburg Concordia plot in Fig. 10b. A lower concordia intercept of 604 ± 50 Ma, ($n=8$) (MSWD = 5.6) is obtained for a discord anchored at 4550 Ma (common Pb; Tatsumoto *et al.* 1973). The weighted average $^{206}\text{Pb}/^{238}\text{U}$ age of 605 ± 17 Ma ($n=8$) (MSWD = 3.1) is calculated for this lower cluster of matrix analyses (Fig. 10c).

The model one solution for the monazites within the garnet, yields an upper intercept age of 1201 ± 57 Ma and a lower intercept of 470 ± 180 Ma ($n=10$) (MSWD of 6.8) (Fig. 10d). The upper intercept age is the best estimate of the original age of the monazites within garnet as it takes into account grains which have undergone minimal Pb loss.

5.2.4 Sample A325-507A

Eighteen analyses were performed on twelve monazite grains from sample A325-507A (Fig. 8c). The targeted monazite grains were predominately hosted within garnet grains. A number of monazite grains located within feldspar grains were analysed; however, with the exception of two grains, these were too small for analysis (size <10 μm with an 8 μm laser beam diameter) and no resolvable parts of the signal could be recovered.

Data from analyses with reliable signals are displayed on a conventional concordia plot in Fig. 9a. A discord yields an upper intercept age of 1388 ± 82 Ma and a lower intercept of 584 ± 120 Ma ($n=13$) (MSWD of 6.8). By plotting only the analyses from monazite grains in garnet, only two analyses (shown as grey ellipses in Fig. 11a) from the feldspar-hosted monazite grains are discounted, and hence the upper and lower intercept age estimates are

very similar. For the monazite in garnet analyses, the upper intercept is 1389 ± 89 Ma and the lower intercept is 578 ± 150 Ma ($n = 11$) (MSWD of 7.7) (Fig. 11b). When the feldspar-hosted analyses are removed, there is no significant difference in the resultant age. The upper intercept age is the best estimate of the age as there exists few concordant grains and takes into account grains that have undergone minimal Pb loss. The lower intercept, whilst within uncertainty of other age estimates from similar samples, is not well constrained enough to give a useable age estimate.

5.2.5 Sample A325-917D

Twenty analyses were conducted on eleven monazite grains from sample A325-917D (Fig. 8d). The targeted monazite grains all occur within the matrix. All of the analyses are shown in a traditional concordia plot (Fig. 12a). The data yields a discord that has upper intercept age of 1187 ± 46 Ma and a lower intercept of 579 ± 120 Ma. The upper intercept is defined by concordant grains. This upper cluster of data was plotted on a Tera-Wasserburg plot (Fig. 12b) and reveals a lower concordia intercept of 1173 ± 50 Ma ($n = 7$) (MSWD = 4.2) for a discord anchored at 4550Ma (common Pb; Tatsumoto *et al.* 1973). This upper cluster produces a weighted average $^{207}\text{Pb}/^{206}\text{Pb}$ age of 1184 ± 40 Ma ($n = 7$) (MSWD = 2.7) (Fig. 12c). The weighted average $^{207}\text{Pb}/^{206}\text{Pb}$ age is comparable the common Pb corrected age; hence it is unlikely that common lead is affecting these analyses (despite some individual analyses having high ^{204}Pb counts per second). Therefore the best approximation for the age of the sample is the weighted average $^{207}\text{Pb}/^{206}\text{Pb}$ age that incorporates a few concordant grains. The lower intercept of the conventional concordia plot (Fig. 12b) is within uncertainty of age estimates from similar samples (above) but there are not enough analyses populating the lower intercept to tightly constrain the age estimate, as indicated by the high uncertainty on the intercept age.

5.2.6 Sample A325-882

Nineteen analyses on sixteen monazite grains were conducted from sample A325-882 (Fig. 8e). All analysed monazite grains were located in the matrix, some in direct contact with ilmenite. All age data are plotted on a conventional concordia diagram in Fig. 13a. Despite the consistent microstructural setting of the targeted monazite grains, a variety of ages emerge. This range becomes apparent by inserting a discord, which yields an upper intercept of 1127 ± 55 Ma and a lower intercept of 552 ± 98 Ma ($n = 19$) (MSWD = 3.8). These analyses define a linear Pb loss trend with concordant to moderately discordant (96-102%) components. The weighted average $^{207}\text{Pb}/^{206}\text{Pb}$ age of the analyses defining the concordant upper age cluster (black ellipses), shown in Fig. 13b, gives an age of 1154 ± 34 Ma ($n = 11$) (MSWD = 1.7). As with other samples, the upper intercept age is the best estimate for this sample, due to these monazites having undergone minimal Pb loss.

5.3 *P-T* estimates

5.3.1 Sample A325-535A

A *P-T* pseudosection for sample A325-535A is shown in Fig. 14a. The peak mineral assemblage, hornblende-clinopyroxene-garnet-plagioclase-quartz-ilmenite-rutile, occurs over a wide stability range in *P-T* space; 500- 850 °C and 7.5- 17 kbar. Such a large range of stability does not place tight constraints on the *P-T* conditions of metamorphism during the Petermann Orogeny. The pseudosection was contoured for the compositions of garnet ($X_{\text{Fe}} = \text{Fe}/\text{Fe} + \text{Mg}$ and $X_{\text{Ca}} = \text{Ca}/\text{Ca} + \text{Mg} + \text{Fe}$) and clinopyroxene ($X_{\text{Fe}} = \text{Fe}/\text{Fe} + \text{Mg}$) in order to further constrain the *P-T* conditions of metamorphism. As a further minimum constraint on *P-T* conditions, average *P-T* calculations (i.e. conventional thermobarometry) using the peak assemblage define *P-T* conditions of 11.5 ± 2.6 kbar and 638 ± 111 °C.

The measured chemistry of garnet shows a decrease in average X_{Ca} values from the cores to the rims of garnet grains of 0.33 to 0.22 (Appendix B). Compositional isopleths show this

corresponds to a decrease in pressure, crossing the rutile-absent line in doing so (figure 14a). The quantitative measurements of X_{Fe} of garnet show a decrease from core to rim from 0.82 to 0.75 (Appendix B). This does not correspond to a comparable area on the constructed pseudosection but if the values are judged qualitatively then this decreasing X_{Fe} value can be attributed to a decrease in pressure and temperature (Fig. 14b). No chemical zonation was measured in the clinopyroxene grains. The X_{Fe} of clinopyroxene is 0.22 (on average), which confines them to the hb-di-pl-ilm-g-q field (Fig. 14c). This data together define a clock-wise P - T path.

5.4 Thermal modelling and garnet diffusion

Models for two garnet profiles were fitted using the diffusion modelling code of Robl *et al.* (2007) (Fig. 15). The first profile (T1) was fitted to a larger garnet ($r = 127.7 \mu\text{m}$) and resulted in a heating duration of 0.1 Ma. The second profile (T2) was fitted to a small garnet ($r = 61.7 \mu\text{m}$) and resulted in a heating duration of 27 Ma. Varying sized garnets were examined in order to examine the effects of mylonisation on the diffusion profiles of garnet grains. Experimentation with a number of diffusion constants was undertaken but differences were negligible, as also documented by Camacho *et al.* (2009).

6. Discussion and conclusion

A thorough understanding of the nature of Ediacaran-Cambrian intracratonic orogenesis in the Musgrave Province still remains an enigma. However, this study has refined the duration and evolution of the Petermann Orogeny by investigation of the pressure-temperature-time evolution, encompassing the integration of *in situ* geochronology, modern metamorphic analysis and diffusion-based cooling rate estimations.

It is clear from visual inspection of the geochronological data set collected that the monazite grains record multiple ages. There seems a distinct cluster from 1201 – 1127 Ma, which correlates to the Mid-Proterozoic Musgrave Orogeny (Gray & Compston 1978; Camacho & Fanning 1995). However, these monazites have clearly undergone resetting, which is apparent by the arrangement of the analyses on a discord. The lower intercept gives an age estimate of 584-579 Ma. This falls within age estimates for the Petermann Orogeny, a 620-530 Ma event. However, no concordant grains from these samples are apparent from the dataset and individual analyses clustered around this lower intercept have large uncertainties. Therefore, whereas a younger event is apparent in these samples, age estimates can only be provided when the data is anchored. However, sample A325-875A contains numerous concordant grains and a cluster of analyses that give a weighted average age of 598 Ma. Whilst slightly older than the anchored lower intercept ages, it is still within uncertainty and can be correlated also to the timing of the Petermann Orogeny. There is no spatial or size relationship between the sample that gave concordant age analyses or a lower intercept age estimating Petermann Orogeny reworking. It can be interpreted that the concordant grains represent grains completely reset during the tectonism. It is also to be noted that sample A325-318 gave a few concordant grains, but the MSWD was too high (MSWD= 5.6) for the data to be reliably justified.

Sample A325-507A records a concordant age single analysis estimate of 1389 ± 89 Ma. This is significantly older than any of the other analyses. This analysis is comparable with U-Pb SHRIMP ages from zircon cores dated by White *et al* (1999) and thus may be indicative of the presence of Mt West orogeny-aged granitic rocks in the study area (White *et al.* 1999; Smithies *et al.* 2010). The study of the felsic orthogneisses in the eastern Musgrave Province gave ages interpreted to be magmatic ages spanning from 1324 ± 12 Ma and 1296 ± 8 Ma.

Rocks corresponding to the Mt West Orogeny are currently only known in the west Musgrave Province.

It is evident that there is very little new monazite growth (reflected by few concordant grains) during the Petermann Orogeny. The presence of partially reset monazites are more common; however, the *in situ* dating has demonstrated that only few were fully reset, due to the preservation of Musgrave Orogeny ages. The resetting of monazite is dependent on Pb diffusion, which is controlled by a number of factors including the presence of fluids, temperature and strain rates (Ayers *et al.* 1999). The lack of fluid present during the Petermann Orogeny is evident by the paucity of hydrous minerals in the resultant metamorphic rocks. Ayers *et al.* (1999) suggests that monazite will coarsen in the presence of fluid. As fluids are sparse, it provides a possibility as to why resetting of existing monazites and the growth of new grains is rare in the Petermann Orogeny.

The peak temperature for Petermann-aged metamorphism is estimated at 638 ± 111 °C. This temperature determines whether Pb diffusion in monazite grains will occur, and induce resetting. It has been suggested that the closure temperature (i.e. the temperature below which Pb diffusion will no longer occur) is in excess of 900 °C for a monazite grain <10 µm (Cherniak *et al.* 2004). Given the low temperature reached during the Petermann Orogeny, this supports the notion that Pb diffusion was sluggish and any resetting was partial.

It is likely then to be the presence of fluids and the temperature of metamorphism during Petermann-aged deformation to be the control. This is supported by the correlation of the occurrence of few concordant grains with the low temperatures these grains experienced and the lack of fluids at the time of deformation. Given this conclusion, it is suggested that the age estimates obtained from concordant grains are to be interpreted as the age of peak

metamorphism. Peak metamorphism is the period of highest temperature and hence more optimum kinetics for lead diffusion and resetting of the U-Pb system of monazite.

Conventional thermobarometric techniques yield pressure-temperature estimates for Petermann-aged metamorphism of 11.5 kbar and 640 °C. This result harmonises with the mineralogical constraints determined by the constructed pseudosection. This pressure and temperature is interpreted to be the peak conditions, as it was determined using analyses from the core of the garnets. The metamorphosed dyke suite from which the average *P-T* constraints were estimated, intruded at *c.* 820Ma and hence only experience Petermann-aged metamorphism. In these dykes, only garnet and clinopyroxene porphyroclasts are large enough to study mineralogical changes through growth by examining core and rim compositions. Furthermore, only the garnet porphyroclasts are zoned, the clinopyroxene porphyroclasts remain compositionally homogenous. The cores of the zoned garnets show higher calcium levels ($X_{Ca}=0.33$) in comparison with the rims ($X_{Ca}=0.22$). This decrease from core to rim is interpreted to be due to the growth of clinopyroxene and plagioclase, which require calcium. This decrease in calcium can be attributed to a decrease in pressure, as garnet will become more enriched in calcium with increasing pressure. This same trend is also seen for the iron levels in garnets, which is also incorporated into the growing clinopyroxene grains. The smaller garnet grains are similar in composition to the large zoned garnet rims, suggesting late growth. Despite there being little to no reaction textures visible in these extremely fine grained rocks; there is further suggestion that the rock underwent extensive overprinting from the start to end of the metamorphic event. This is supported by the very low abundance of rutile in the sample A325-535A. Whilst it is interpreted to have been present at the metamorphic peak, on the basis of the calculated pseudosection, the compositional contours give evidence for the retrograde path crossing the ru-absent line. It is

therefore interpreted that the mineral assemblage seen in these rocks is dominated by the retrogressed assemblage, as opposed to the peak.

Sample A325- 907E produces garnet profiles that have X_{Ca} values that increase from core to rim. This zonation pattern contrasts the one observed in sample A325- 535A. The profiles also show variable core compositions (Fig. 15), which have been attributed to the differing size of garnet porphyroblasts. The smaller garnet ($r = 61.7 \mu\text{m}$) is interpreted to have a core composition that has been reset whilst the larger garnet ($r = 127.7 \mu\text{m}$) probably preserves pre-Petermann reworking X_{Ca} values in the core. Consequently, the profiles T1 and T2 return contrasting results for the duration of metamorphism. Spear (1991) demonstrates this theory experimentally in an analogous study using Mg-Fe exchange in garnet- biotite pairs (Fig. 16). The larger garnets record less of the thermal history due to the mechanical breakdown of the diffusional rims. It is interpreted that the small garnets are remnants, broken from the larger garnet grains. Following this logic, it is apparent that the larger grains have had their diffusive rims mechanically worn away to produce these smaller garnets. These smaller garnets have then independently produced diffusion profiles. As a result, the larger garnet grains do not produce diffusion rims that record the full metamorphic interval, rather the small garnets will give a minimum time for metamorphism. As no one garnet diffusion profile can accurately determine the duration of metamorphism for this such reason, a coupled approach was taken. This modelling returns a minimum duration of 27 Myr. This duration has been interpreted to be the duration of prograde metamorphism due to the X_{Ca} of garnet increasing from rim to core. As pressure increases, garnet becomes more enriched in calcium (as shown by calculated compositional isopleths in Fig. 14b).

As the geochronological data collected is an estimate of peak metamorphism, it then suggests that the onset of burial occurred *c.* 625 Ma. Previous studies have used sedimentological

evidence and basin structure from the Officer Basin to estimate the onset of the Petermann Orogeny and have proposed time frames from 650– 540 Ma (Hoskins & Lemon 1995; Lindsay & Leven 1996; Calver & Lindsay 1998; Wade *et al.* 2006). Despite the near 100 Myr spread in commencement ages, the data from this study correlates well with these estimates.

More recently, much shorter (<1 Ma) durations have been proposed for the prograde phase of metamorphism (Camacho *et al.* 2009). Primary evidence given for a short-lived event is under-developed diffusion profiles in garnet grains. Despite producing mathematically and statistically meaningful results, only large (~500 μm) garnets were examined and hence geologically relevant answers were not obtained. Had various sized garnets been examined (as in this study) then it would have become apparent that the record of metamorphism is not complete in all garnets. The results from the study of Camacho *et al.* (2009) and from this study show that isolated results must be interpreted with caution and a more integrated approach is more suitable for this region.

Curiously, there appears to be no record of the cooling history (retrograde path) of the metamorphic event in the diffusion profiles of these garnets. T2 however, may be an exception. From examination of the X_{Ca} profile, a slight decrease in X_{Ca} at the very rim may represent a decrease in pressure, i.e. the cooling history (retrograde path). The explanation why this near-rim change is visible in T2 and not T1 is once again due to the volume of the garnet, analogous to the record of the heating path.

There exists several plausible situations to why no cooling/exhumation history is preserved in the garnet grains. Firstly, the under-developed profiles (or lack of in larger garnets) may suggest that cooling occurred over a very short time-span. A fast exhumation would account for the lack of elemental diffusion and overprinting of the prograde history. Despite this, this conclusion is not consistent with data collected from further west in the Musgrave Province.

Studies by Raimondo *et al.* (2009, 2010) have determined cooling rates using titanite data of ~1.8- 5.8 °C/Myr. Peak temperatures of 733 ± 23 were obtained at *c.* 540 Ma in the western Mann Ranges and complementary titanite cooling ages place a constraint of 600-650 °C at 521 ± 11 Ma (*c.* 520 Ma). This therefore defines a cooling rate of ~3.75-5 °C/Myr for this area (Walsh 2010, unpublished data). Furthermore, sedimentological studies from the Officer Basin (Wade *et al.* 2005) have argued that orogenesis was either a long-lived events or a series of events that spanned for greater than 70 Myr.

Another possibility is that the garnet grains, although given the time to diffuse, were unable to record the event. This could occur for a number of reasons. First relates to the rate of diffusion of the cations involved. Calcium is known as a “sluggish” diffuser due to its large cation size, with respect to other diffusing elements in garnet such as magnesium and iron (Schwandt *et al.* 1996; Carlson 2006). However, it has been shown experimentally by Yund & Tullis (1991) that dislocation creep can cause an increase in calcium mobility. During uplift and mylonisation of these rocks, dislocation creep would probably have been prominent and hence would have allowed for Ca diffusion and resetting of prograde zoning, in particular in response to migrating grain boundaries of recrystallising plagioclase. The notion of closure temperature could have also had an effect on the ability of garnet to record the cooling history. This concept, although originally termed for use in systems used for dating, can also be applied to chemical zonation. Caddick *et al.* (2010) declared that chemical zoning is modified at temperatures above closure temperature and that diffusivity of divalent cations (Ca, Mg, Fe, Mn) is strongly temperature dependent. Taking into account the size of the garnet grains analysed, diameter =123.4 μm and 255.4 μm , it is estimated that peak temperature would have had to remain for ~25 Myr and >50 Myr for the prograde zoning to be reset (Caddick *et al.* 2010). Based on the observation that little to no diffusion profile has been preserved of the cooling history, one can assume that the rocks cooled quickly over the

short temperature interval between peak and closure temperature. Had they cooled slowly over this interval, then diffusion would have been allowed to occur and the prograde zoning reset. No constraint can be given though for the temperature interval below closure temperature.

In light of the cooling data collected from the western Musgrave Province, coupled with sedimentological evidence from the Officer Basin, it seems unlikely that cooling/exhumation occurred over a short time period. Clear evidence provided through titanite cooling ages and U-Pb geochronology provides a sound argument for long-lived orogenesis in the Petermann Orogeny. Following the discussion of closure temperatures of garnet in relation to diffusion, it does seem more plausible that this is the cause for preservation of prograde zoning in the garnet grains from the Amata region. Whilst the low peak temperature (and a long burial history) has allowed for quantitative analysis of the prograde path of metamorphism it does not allow for garnet zonation to be used a proxy for cooling rates (in this case) or an exhumation history. Therefore, research into cooling rates in the Amata region in the future must be explored using a different technique, such as mineral cooling ages, which has shown to be successful as a tool in the western Musgrave Province (Raimondo *et al.* 2009, 2010).

The pressure-temperature-time evolution investigation into the Petermann Orogeny has shown a clock-wise P - T path for the metamorphic evolution of the orogen, with a minimum heating/burial duration of ~27 Myr, reaching peak conditions of ~640 °C and ~11.5 kbar at *c.* 598 Ma. This, coupled with thermochronological data from the western Musgrave Province and sedimentological evidence from the Officer Basin to the south, disproves the theory that these eclogite facies, low geothermal gradient rocks were the result of a short-lived tectonothermal event, namely shear heating (Camacho *et al.* 2009). This study cannot

definitively model the metamorphic and deformation evolution of these rocks but provides the first integrated results allowing for appraisal of two contradicting models for the region.

7. Acknowledgements

Thanks go to my supervisors David Kelsey and Martin Hand for their handy geological advice and support. Also, to Justin Payne and Kathryn Cutts whose help has been invaluable; I am very grateful. Thanks also to Ben Wade, Angus Netting and the staff at Adelaide Microscopy who have been very patient this year and whom I have learnt so much from. To Alec Walsh and the honours class of 2010 for their insightful geological conversations and helpful advice.

8. Appendices

Appendix A - Sample lithologies, petrological groups and data collected.

Sample Number	Petrological group	Lithological Unit (as in Fig. 3)	Data
A340 63	Mafic mylonite	Altered granulite and gneissic granulite	
A340 103	Mafic mylonite	Altered granulite and gneissic granulite	
A340 42	Felsic mylonite	Altered granulite and gneissic granulite	
A340 65	Mafic mylonite	Altered granulite and gneissic granulite	
A325 507A	Felsic mylonite	Altered granulite and gneissic granulite	SEM Images, LA-ICPMS monazite data
A325 1011	Mafic mylonite	Altered granulite and gneissic granulite	SEM images
A325 1025B	Mafic mylonite	Altered granulite and gneissic granulite	
A325 1059	Mafic mylonite	Altered granulite and gneissic granulite	
A325 1096A	Coronitic cpx-bearing mylonite	Birkgate Complex: gneiss of granulite and amphibolite facies	Electron microprobe data
A325 1175	Felsic mylonite	Birkgate Complex: gneiss of granulite and amphibolite facies	
A325 1573B	Mafic mylonite	Mylonites and cataclasites including the Woodroffe Thrust	
A325 1848	Coronitic cpx-bearing mylonite	Birkgate Complex: gneiss of granulite and amphibolite facies	
A325 1868	Mafic mylonite	Birkgate Complex: gneiss of granulite and amphibolite facies	
A325 318	Felsic mylonite	Gneissic granite	SEM images, LA-ICPMS monazite data
A325 322	Mafic mylonite	Gneissic granite	
A325 445	Mafic mylonite	Gneissic granite	Electron microprobe data
A325 469	Coronitic cpx-bearing mylonite	Altered granulite and gneissic granulite	
A325 470	Coronitic cpx-bearing mylonite	Altered granulite and gneissic granulite	SEM images
A325 500	Felsic mylonite	Altered granulite and gneissic granulite	
A325 507B	Felsic mylonite	Altered granulite and gneissic granulite	
A325 507C	Felsic mylonite	Altered granulite and gneissic granulite	Electron microprobe data
A325 516	Felsic mylonite	Altered granulite and gneissic granulite	
A325 535A	Hb-bearing mylonites	Altered basic dyke in shear zones	Bulk composition, Electron microprobe data
A325 535B	Hb-bearing mylonites	Altered basic dyke in shear zones	Bulk composition
A325 576	Felsic mylonite	Gneissic granite	
A325 59	Coronitic cpx-bearing mylonite	Altered granulite and gneissic granulite	
A325 663	Felsic mylonite	Gneissic granite	
A325 672	Felsic mylonite	Gneissic granite	

Sample Number	Petrological group	Lithological Unit (as in Fig. 3)	Data
A325 673	Mafic mylonite	Gneissic granite	
A325 705B	Coronitic cpx-bearing mylonite	Birksgate Complex: gneiss of granulite and amphibolite facies	Electron microprobe data
A325 721	Mafic mylonite	Birksgate Complex: gneiss of granulite and amphibolite facies	
A325 764	Hb-bearing mylonites	Birksgate Complex: gneiss of granulite and amphibolite facies	
A325 777C	Mafic mylonite	Birksgate Complex: gneiss of granulite and amphibolite facies	
A325 783A	Mafic mylonite	Birksgate Complex: gneiss of granulite and amphibolite facies	
A325 823B	Mafic mylonite	Birksgate Complex: gneiss of granulite and amphibolite facies	
A325 874	Hb-bearing mylonites	Birksgate Complex: gneiss of granulite and amphibolite facies	
A325 875A	Felsic mylonite	Birksgate Complex: gneiss of granulite and amphibolite facies	SEM images, LA-ICPMS monazite data, Electron microprobe data
A325 882	Felsic mylonite	Birksgate Complex: gneiss of granulite and amphibolite facies	SEM images, LA-ICPMS monazite data
A325 900A	Felsic mylonite	Birksgate Complex: gneiss of granulite and amphibolite facies	
A325 900B	Felsic mylonite	Birksgate Complex: gneiss of granulite and amphibolite facies	
A325 903	Mafic mylonite	Birksgate Complex: gneiss of granulite and amphibolite facies	
A325 907E	Felsic mylonite	Birksgate Complex: gneiss of granulite and amphibolite facies	Electron microprobe data
A325 907K	Dolerite dyke	Altered basic dyke in shear zones	Bulk composition
A325 907Q	Dolerite dyke	Altered basic dyke in shear zones	Bulk composition, Electron microprobe data
A325 911	Felsic mylonite	Birksgate Complex: gneiss of granulite and amphibolite facies	Electron microprobe data
A325 912B	Dolerite dyke	Altered basic dyke in shear zones	
A325 912G	Dolerite dyke	Altered basic dyke in shear zones	
A325 912I	Dolerite dyke	Altered basic dyke in shear zones	
A325 912L	Dolerite dyke	Altered basic dyke in shear zones	
A325 912M	Dolerite dyke	Altered basic dyke in shear zones	
A325 914	Mafic mylonite	Birksgate Complex: gneiss of granulite and amphibolite facies	
A325 917D	Felsic mylonite	Birksgate Complex: gneiss of granulite and amphibolite facies	SEM images, LA-ICPMS monazite data
A325 919	Hb-bearing mylonites	Birksgate Complex: gneiss of granulite and amphibolite facies	
A325 936G	Hb-bearing mylonites	Birksgate Complex: gneiss of granulite and amphibolite facies	
A325 936E	Hb-bearing mylonites	Birksgate Complex: gneiss of granulite and amphibolite facies	
BO M9Z 93A	Hb-bearing mylonites	Birksgate Complex: gneiss of granulite and amphibolite facies	

Appendix B - Microprobe analyses

<i>Sample A325-445</i>							
	Bi	Gt new	Pl rim	Pl core	Opx	Ksp	Ilm
SiO2	38.55	40.65	59.57	60.21	50.07	64.79	0.01
TiO2	4.25	0.03	0.05	0.03	0.26	0.02	52.01
Al2O3	12.31	20.08	23.49	23.43	0.97	18.20	0.00
Cr2O3	0.02	0.00	0.05	0.00	0.00	0.01	0.01
FeO	13.42	28.12	2.57	0.03	27.88	0.02	44.90
MnO	0.00	1.28	0.06	0.03	0.83	0.05	0.95
MgO	16.52	3.32	0.11	0.02	18.42	0.02	0.08
ZnO	0.15	0.04	0.00	0.11	0.16	0.00	0.30
CaO	0.01	7.16	5.41	5.68	0.59	0.07	0.02
Na2O	0.03	0.03	8.78	8.58	0.06	1.26	0.02
K2O	9.96	0.00	0.49	0.19	0.00	14.95	0.00
NiO	0.00	0.00	0.00	0.00	0.00	0.00	0.00
Total	95.23	100.71	100.57	98.32	99.25	99.38	98.32
No. Oxygens	11.00	12.00	8.00	8.00	6.00	8.00	3.00
Si	2.87	3.17	2.68	2.73	1.93	3.00	0.00
Ti	0.24	0.00	0.00	0.00	0.01	0.00	1.00
Al	1.08	1.84	1.25	1.25	0.04	0.99	0.00
Cr	0.00	0.00	0.00	0.00	0.00	0.00	0.00
Fe3+	0.00	0.00	0.00	0.00	0.08	0.00	0.00
Fe2+	0.84	1.83	0.10	0.00	0.81	0.00	0.96
Mn2+	0.00	0.08	0.00	0.00	0.03	0.00	0.02
Mg	1.84	0.39	0.01	0.00	1.06	0.00	0.00
Zn	0.01	0.00	0.00	0.00	0.00	0.00	0.01
Ca	0.00	0.60	0.26	0.28	0.02	0.00	0.00
Na	0.00	0.01	0.77	0.75	0.00	0.11	0.00
K	0.95	0.00	0.03	0.01	0.00	0.88	0.00
Ni	0.00	0.00	0.00	0.00	0.00	0.00	0.00
Sum	7.82	7.91	5.09	5.03	4.00	5.00	2.00

<i>Sample A325-911</i>						
	Plag rim	Plag core	Gt rim	Gt core	Ttn	Ksp
SiO2	61.63	60.74	38.70	38.11	38.60	62.84
TiO2	0.01	0.01	0.04	0.04	0.00	0.10
Al2O3	23.64	23.20	22.07	21.97	21.43	18.75
Cr2O3	0.03	0.02	0.03	0.03	0.00	0.04
FeO	0.02	0.18	24.35	24.84	22.07	0.04
MnO	0.02	0.00	1.09	1.13	1.08	0.01
MgO	0.00	0.00	11.97	11.91	8.17	0.01
ZnO	0.13	0.00	0.00	0.00	0.05	0.00
CaO	5.59	5.60	1.50	1.17	7.96	0.92
Na2O	8.49	8.81	0.02	0.00	0.01	2.92
K2O	0.24	0.21	0.02	0.00	0.00	11.67
NiO	0.00	0.00	0.00	0.00	0.00	0.00
Total	99.81	98.76	99.78	99.20	99.37	97.30
No. Oxygens	8.00	8.00	12.00	12.00	5.00	8.00
Si	2.75	2.74	2.95	2.93	1.24	2.95
Ti	0.00	0.00	0.00	0.00	0.00	0.00
Al	1.24	1.23	1.98	1.99	0.81	1.04
Cr	0.00	0.00	0.00	0.00	0.00	0.00
Fe3+	0.00	0.00	0.00	0.00	0.00	0.00
Fe2+	0.00	0.01	1.55	1.60	0.59	0.00
Mn2+	0.00	0.00	0.07	0.07	0.03	0.00
Mg	0.00	0.00	1.36	1.37	0.39	0.00
Zn	0.00	0.00	0.00	0.00	0.00	0.00
Ca	0.27	0.27	0.12	0.10	0.27	0.05
Na	0.73	0.77	0.00	0.00	0.00	0.27
K	0.01	0.01	0.00	0.00	0.00	0.70
Ni	0.00	0.00	0.00	0.00	0.00	0.00
Sum	5.01	5.03	8.05	8.07	3.35	5.01

Sample A325-535A										
	Cpx rim	Cpx core	Gt rim	Gt core	Pl	Cpx new	Ttn	Gt new	hb	
SiO2	52.89	53.25	37.07	37.61	64.18	54.55	30.69	38.13	41.19	
TiO2	0.31	0.12	0.06	0.06	0.08	0.13	37.19	0.04	0.27	
Al2O3	3.90	2.70	21.17	21.24	21.82	2.88	1.91	21.22	15.50	
Cr2O3	0.06	0.12	0.00	0.03	0.00	0.02	0.00	0.00	0.00	
FeO	9.01	9.52	27.21	26.18	0.27	7.66	0.93	27.05	22.76	
MnO	0.04	0.00	0.46	0.61	0.02	0.07	0.03	0.44	0.34	
MgO	11.84	11.79	4.76	3.09	0.00	11.99	0.00	4.89	6.85	
ZnO	0.15	0.13	0.05	0.00	0.13	0.13	0.00	0.00	0.00	
CaO	18.69	19.43	7.85	11.09	2.76	19.89	27.51	8.27	10.15	
Na2O	2.37	2.61	0.00	0.04	9.71	1.99	0.24	0.06	0.41	
K2O	0.13	0.01	0.00	0.01	0.14	0.00	0.01	0.01	0.35	
NiO	0.00	0.00	0.00	0.00	0.00	0.00	0.00	0.00	0.00	
Total	99.39	99.67	98.64	99.95	99.13	99.31	98.51	100.12	97.82	
No. Oxygens	6.00	6.00	12.00	12.00	8.00	6.00	5.00	12.00	23.00	
Si	1.96	1.97	2.96	2.97	2.85	2.03	1.01	2.99	6.27	
Ti	0.01	0.00	0.00	0.00	0.00	0.00	0.92	0.00	0.03	
Al	0.17	0.12	1.99	1.98	1.14	0.13	0.07	1.96	2.78	
Cr	0.00	0.00	0.00	0.00	0.00	0.00	0.00	0.00	0.00	
Fe3+	0.06	0.12	0.00	0.00	0.00	0.00	0.00	0.00	0.00	
Fe2+	0.21	0.17	1.82	1.73	0.01	0.24	0.03	1.77	2.89	
Mn2+	0.00	0.00	0.03	0.04	0.00	0.00	0.00	0.03	0.04	
Mg	0.65	0.65	0.57	0.36	0.00	0.66	0.00	0.57	1.55	
Zn	0.00	0.00	0.00	0.00	0.00	0.00	0.00	0.00	0.00	
Ca	0.74	0.77	0.67	0.94	0.13	0.79	0.97	0.69	1.65	
Na	0.17	0.19	0.00	0.01	0.84	0.14	0.02	0.01	0.12	
K	0.01	0.00	0.00	0.00	0.01	0.00	0.00	0.00	0.07	
Ni	0.00	0.00	0.00	0.00	0.00	0.00	0.00	0.00	0.00	
Sum	4.00	4.00	8.04	8.04	4.99	4.00	3.03	8.03	15.41	

Sample A325-907Q						
	Cpx rim	Cpx core	Cpx new	Gt new	Pl	
SiO2	52.32	53.08	52.30	38.23	64.06	
TiO2	0.17	1.12	0.20	0.05	0.02	
Al2O3	3.93	3.11	5.04	21.52	21.43	
Cr2O3	0.14	0.12	0.06	0.00	0.00	
FeO	7.31	7.62	7.52	25.48	0.48	
MnO	0.02	0.02	0.00	0.61	0.02	
MgO	12.05	12.53	11.61	5.80	0.01	
ZnO	0.05	0.08	0.15	0.03	0.12	
CaO	19.66	19.72	19.17	8.47	2.96	
Na2O	2.84	2.69	3.06	0.02	10.36	
K2O	0.01	0.01	0.02	0.00	0.26	
NiO	0.00	0.00	0.00	0.00	0.00	
Total	98.50	100.09	99.13	100.21	99.72	
No. Oxygens	6.00	6.00	6.00	12.00	8.00	
Si	1.94	1.95	1.93	2.98	2.85	
Ti	0.00	0.03	0.01	0.00	0.00	
Al	0.17	0.13	0.22	1.97	1.12	
Cr	0.00	0.00	0.00	0.00	0.00	
Fe3+	0.14	0.10	0.14	0.00	0.00	
Fe2+	0.09	0.13	0.09	1.66	0.02	
Mn2+	0.00	0.00	0.00	0.04	0.00	
Mg	0.67	0.68	0.64	0.67	0.00	
Zn	0.00	0.00	0.00	0.00	0.00	
Ca	0.78	0.77	0.76	0.71	0.14	
Na	0.20	0.19	0.22	0.00	0.89	
K	0.00	0.00	0.00	0.00	0.01	
Ni	0.00	0.00	0.00	0.00	0.00	
Sum	4.00	4.00	4.00	8.04	5.04	

<i>Sample A325-907E</i>					
	Gt rim	Gt core	Pl	Gt new	Ksp
SiO2	37.65	38.68	62.81	38.91	64.30
TiO2	0.00	0.00	0.00	0.02	0.09
Al2O3	21.70	21.27	22.37	21.64	18.22
Cr2O3	0.05	0.02	0.00	0.04	0.05
FeO	23.44	25.93	0.07	23.62	0.64
MnO	1.12	1.46	0.00	0.83	0.00
MgO	7.91	10.33	0.00	7.53	0.01
ZnO	0.00	0.00	0.00	0.03	0.00
CaO	6.64	2.00	4.40	7.74	1.03
Na2O	0.00	0.03	9.18	0.00	2.27
K2O	0.02	0.02	0.28	0.01	12.25
NiO	0.00	0.00	0.00	0.00	0.00
Total	98.54	99.75	99.12	100.37	98.85
No. Oxygens	12.00	12.00	8.00	12.00	8.00
Si	2.95	2.98	2.81	2.99	2.98
Ti	0.00	0.00	0.00	0.00	0.00
Al	2.00	1.93	1.18	1.96	0.99
Cr	0.00	0.00	0.00	0.00	0.00
Fe3+	0.00	0.00	0.00	0.00	0.00
Fe2+	1.54	1.67	0.00	1.52	0.02
Mn2+	0.07	0.10	0.00	0.05	0.00
Mg	0.92	1.19	0.00	0.86	0.00
Zn	0.00	0.00	0.00	0.00	0.00
Ca	0.56	0.17	0.21	0.64	0.05
Na	0.00	0.00	0.80	0.00	0.20
K	0.00	0.00	0.02	0.00	0.72
Ni	0.00	0.00	0.00	0.00	0.00
Sum	8.05	8.05	5.01	8.03	4.98

<i>Sample A325-875A</i>							
	Plag	Gt rim	Gt core	Ksp	Gt new	Ilm	Ru
SiO2	64.47	37.97	38.96	64.01	0.07	98.36	38.27
TiO2	0.01	0.09	0.04	0.09	98.88	0.04	0.12
Al2O3	20.99	21.75	21.77	18.42	0.00	0.00	21.79
Cr2O3	0.00	0.00	0.07	0.00	0.09	0.01	0.15
FeO	0.19	24.16	26.31	0.32	0.07	0.07	22.00
MnO	0.04	1.73	1.65	0.02	0.00	0.03	1.06
MgO	0.01	7.92	9.83	0.00	0.00	0.00	8.10
ZnO	0.09	0.00	0.05	0.08	0.00	0.07	0.00
CaO	3.60	5.69	1.63	0.12	0.12	0.02	6.76
Na2O	8.85	0.04	0.00	1.37	0.00	0.01	0.02
K2O	1.60	0.01	0.02	14.67	0.02	0.00	0.02
NiO	0.00	0.00	0.00	0.00	0.00	0.00	0.00
Total	99.85	99.36	100.33	99.10	99.25	98.62	98.29
No. Oxygens	8.00	12.00	12.00	8.00	12.00	3.00	2.00
Si	2.87	2.96	2.99	2.98	0.01	2.00	0.50
Ti	0.00	0.01	0.00	0.00	5.98	0.00	0.00
Al	1.10	2.00	1.97	1.01	0.00	0.00	0.33
Cr	0.00	0.00	0.00	0.00	0.01	0.00	0.00
Fe3+	0.00	0.00	0.00	0.00	0.00	0.00	0.00
Fe2+	0.01	1.57	1.69	0.01	0.00	0.00	0.24
Mn2+	0.00	0.11	0.11	0.00	0.00	0.00	0.01
Mg	0.00	0.92	1.12	0.00	0.00	0.00	0.16
Zn	0.00	0.00	0.00	0.00	0.00	0.00	0.00
Ca	0.17	0.47	0.13	0.01	0.01	0.00	0.09
Na	0.76	0.01	0.00	0.12	0.00	0.00	0.00
K	0.09	0.00	0.00	0.87	0.00	0.00	0.00
Ni	0.00	0.00	0.00	0.00	0.00	0.00	0.00
Sum	5.01	8.04	8.02	5.01	6.01	2.00	1.33

<i>Sample A325-705A</i>							
	Gt	Plag	Ksp	Ilm	Opx	Cpx Rim	Cpx Core
SiO2	37.90	54.65	64.38	0.05	53.50	53.73	52.10
TiO2	0.09	0.03	0.01	44.85	0.00	0.17	0.38
Al2O3	20.66	33.67	18.36	0.00	1.39	2.47	2.75
Cr2O3	0.00	0.00	0.00	0.02	0.01	0.00	0.06
FeO	25.93	0.39	0.51	52.93	24.30	8.58	10.72
MnO	0.35	0.00	0.00	0.35	0.99	0.17	0.87
MgO	2.55	0.00	0.00	0.56	21.35	12.87	13.03
ZnO	0.04	0.00	0.05	0.13	0.09	0.00	0.08
CaO	13.45	6.20	0.13	0.02	0.27	21.75	21.21
Na2O	0.04	5.84	0.80	0.01	0.02	1.85	0.53
K2O	0.01	0.10	15.85	0.00	0.00	0.00	0.00
NiO	0.00	0.00	0.00	0.00	0.00	0.00	0.00
Total	101.02	100.88	100.09	98.91	101.92	101.59	101.71
No. Oxygens	12.00	8.00	8.00	3.00	6.00	6.00	6.00
Si	2.98	2.41	2.98	0.00	1.97	1.95	1.92
Ti	0.01	0.00	0.00	0.85	0.00	0.00	0.01
Al	1.91	1.75	1.00	0.00	0.06	0.11	0.12
Cr	0.00	0.00	0.00	0.00	0.00	0.00	0.00
Fe3+	0.00	0.00	0.00	0.30	0.00	0.11	0.06
Fe2+	1.70	0.01	0.02	0.82	0.75	0.15	0.27
Mn2+	0.02	0.00	0.00	0.01	0.03	0.01	0.03
Mg	0.30	0.00	0.00	0.02	1.17	0.70	0.72
Zn	0.00	0.00	0.00	0.00	0.00	0.00	0.00
Ca	1.13	0.29	0.01	0.00	0.01	0.85	0.84
Na	0.01	0.50	0.07	0.00	0.00	0.13	0.04
K	0.00	0.01	0.94	0.00	0.00	0.00	0.00
Ni	0.00	0.00	0.00	0.00	0.00	0.00	0.00
Sum	8.06	4.97	5.02	2.00	4.00	4.00	4.00

<i>Sample A325-507C</i>					
	Gt rim	Gt core	Ksp	Plag	Ilm
SiO2	38.06	38.57	65.00	65.33	0.03
TiO2	0.02	0.04	0.01	0.02	47.78
Al2O3	21.81	21.92	20.50	20.90	0.00
Cr2O3	0.08	0.04	0.04	0.00	0.04
FeO	25.29	26.03	0.25	0.14	49.09
MnO	1.35	1.27	0.00	0.01	0.20
MgO	10.56	11.23	0.09	0.00	0.03
ZnO	0.00	0.03	0.00	0.01	0.16
CaO	2.16	0.97	1.92	2.28	0.00
Na2O	0.00	0.00	5.39	6.12	0.00
K2O	0.03	0.04	6.93	6.35	0.01
NiO	0.00	0.00	0.00	0.00	0.00
Total	99.37	100.15	100.14	101.17	97.34
No. Oxygens	12.00	12.00	8.00	8.00	3.00
Si	2.94	2.95	2.92	2.90	0.00
Ti	0.00	0.00	0.00	0.00	0.93
Al	1.99	1.98	1.08	1.09	0.00
Cr	0.01	0.00	0.00	0.00	0.00
Fe3+	0.00	0.00	0.00	0.00	0.14
Fe2+	1.64	1.67	0.01	0.01	0.92
Mn2+	0.09	0.08	0.00	0.00	0.00
Mg	1.22	1.28	0.01	0.00	0.00
Zn	0.00	0.00	0.00	0.00	0.00
Ca	0.18	0.08	0.09	0.11	0.00
Na	0.00	0.00	0.47	0.53	0.00
K	0.00	0.00	0.40	0.36	0.00
Ni	0.00	0.00	0.00	0.00	0.00
Sum	8.06	8.06	4.97	5.00	2.00

Sample A325-1096A								
	Opx	Cpx	Gt	Ru	Bi	Ilm	Ksp	Pl
SiO2	51.92	51.92	39.36	0.10	38.66	0.02	64.43	59.73
TiO2	0.04	0.34	0.02	99.36	3.87	52.16	0.01	0.00
Al2O3	2.78	6.37	21.66	0.00	15.24	0.00	18.54	24.96
Cr2O3	0.11	0.15	0.02	0.19	0.08	0.34	0.02	0.03
FeO	22.16	6.03	23.65	0.74	12.06	44.23	0.68	0.08
MnO	0.33	0.05	0.57	0.04	0.02	0.06	0.00	0.00
MgO	23.35	12.49	7.35	0.00	18.09	1.74	0.00	0.00
ZnO	0.06	0.16	0.00	0.00	0.01	0.00	0.00	0.00
CaO	0.21	21.21	8.76	0.26	0.08	0.00	0.07	7.35
Na2O	0.01	2.19	0.03	0.00	0.06	0.01	1.01	7.46
K2O	0.00	0.00	0.00	0.09	9.79	0.01	15.27	0.50
NiO	0.00	0.00	0.00	0.00	0.00	0.00	0.00	0.00
Totals	100.97	100.92	101.42	100.78	97.97	98.58	100.04	100.11
No. Oxygens	6.00	6.00	12.00	2.00	11.00	3.00	8.00	8.00
Si	1.90	1.88	3.00	0.00	2.77	0.00	2.98	2.67
Ti	0.00	0.01	0.00	0.99	0.21	0.99	0.00	0.00
Al	0.12	0.27	1.94	0.00	1.29	0.00	1.01	1.31
Cr	0.00	0.00	0.00	0.00	0.00	0.01	0.00	0.00
Fe3+	0.07	0.10	0.00	0.00	0.00	0.01	0.00	0.00
Fe2+	0.61	0.08	1.50	0.01	0.72	0.92	0.03	0.00
Mn2+	0.01	0.00	0.04	0.00	0.00	0.00	0.00	0.00
Mg	1.27	0.67	0.83	0.00	1.93	0.07	0.00	0.00
Zn	0.00	0.00	0.00	0.00	0.00	0.00	0.00	0.00
Ca	0.01	0.82	0.71	0.00	0.01	0.00	0.00	0.35
Na	0.00	0.15	0.00	0.00	0.01	0.00	0.09	0.65
K	0.00	0.00	0.00	0.00	0.89	0.00	0.90	0.03
Ni	0.00	0.00	0.00	0.00	0.00	0.00	0.00	0.00
Sum	4.00	4.00	8.03	1.01	7.83	2.00	5.01	5.01

9. References

- AITKEN A. 2008. The analytical of tectonic systems using potential fields: the Musgrave Province, central Australia. PhD thesis, School of Geosciences, Monash University, Melbourne (unpubl.).
- ALEINIKOFF J. N., SCHENCK W. S., PLANK M. O., SROGI L., FANNING C. M., KAMO S. L. & BOSBYSELL H. 2006. Deciphering igneous and metamorphic events in high-grade rocks of the Wilmington Complex, Delaware: Morphology, cathodoluminescence and backscattered electron zoning, and SHRIMP U-Pb geochronology of zircon and monazite. *Geological Society of America Bulletin* **118**, 39-64.
- AYERS J. C., MILLER C., GORISCH B. & MILLEMAN J. 1999. Textural development of monazite during high-grade metamorphism; hydrothermal growth kinetics, with implications for U, Th-Pb geochronology. *American Mineralogist* **84**, 1766-1780.
- CADDICK M. J., KONOPÁSEK J. & THOMPSON A. B. 2010. Preservation of garnet growth zoning and the duration of prograde metamorphism. *Journal of Petrology* **51**, 2327- 2347.
- CALVER C. R. & LINDSAY J. F. 1998. Ediacarian sequence and isotope stratigraphy of the Officer Basin, South Australia. *Australian Journal of Earth Sciences: An International Geoscience Journal of the Geological Society of Australia* **45**, 513 - 532.
- CAMACHO A., COMPSTON W., MCCULLOCH M. & MCDUGALL I. 1997. Timing and exhumation of eclogite facies shear zones, Musgrave Block, central Australia. *Journal of Metamorphic Geology* **15**, 735-751.
- CAMACHO A. & FANNING C. M. 1995. Some isotopic constraints on the evolution of the granulite and upper amphibolite facies terranes in the eastern Musgrave Block, central Australia. *Precambrian Research* **71**, 155-181.
- CAMACHO A. & MCDUGALL I. 2000. Intracratonic, strike-slip partitioned transpression formation and exhumation of eclogite facies rocks: an example from the Musgrave Australia. *Tectonics* **19**, 978-996.
- CAMACHO A., YANG P. & FREDERIKSEN A. 2009. Constraints from diffusion profiles on the duration of high-strain deformation in thickened crust. *Geology* **37**, 755-758.
- CARLSON W. D. 2006. Rates of Fe, Mg, Mn, and Ca diffusion in garnet. *American Mineralogist* **91**, 1-11.
- CHERNAK D. J., WATSON E. B., GROVE M. & HARRISON T. M. 2004. Pb diffusion in monazite: a combined RBS/SIMS study. *Geochimica et Cosmochimica Acta* **68**, 829-840.
- COLLERSON K. 1972. High grade metamorphic and structural relationships near Amata, Musgrave Ranges, central Australia. Ph.D thesis, University of Adelaide, Adelaide (unpubl.).
- DIENER J. F. A., POWELL R., WHITE R. W. & HOLLAND T. J. B. 2007. A new thermodynamic model for clino- and orthoamphiboles in the system Na₂O–CaO–FeO–MgO–Al₂O₃–SiO₂–H₂O–O. *Journal of Metamorphic Geology* **25**, 631-656.
- DODSON M. H. 1973. Closure temperature in cooling geochronological and petrological systems. *Contributions to Mineralogy and Petrology* **40**, 259-274.
- DROOP G. T. R. 1987. A general equation for estimating Fe³⁺ concentrations in ferromagnesian silicates and oxides from microprobe analysis, using stoichiometric criteria *Mineralogical Magazine* **51**, 431 - 435.
- ELLIS D. J. & MABOKO M. A. H. 1992. Precambrian tectonics and the physicochemical evolution of the continental crust. I. The gabbro-eclogite transition revisited. *Precambrian Research* **55**, 491-506.
- EVINS P. M., SMITHIES R. H., HOWARD H. M., KIRKLAND C. L., WINGATE M. T. D. & BODORKOS S. 2010. Devil in the detail; The 1150-1000 Ma magmatic and structural evolution of the Ngaanyatjarra Rift, west Musgrave Province, Central Australia. *Precambrian Research* **183**, 572-588.

- FLÖTTMANN T. & HAND M. 1999. Folded basement-cored tectonic wedges along the northern edge of the Amadeus Basin, Central Australia: evaluation of orogenic shortening. *Journal of Structural Geology* **21**, 399-412.
- FLÖTTMANN T., HAND M., CLOSE D., EDGOOSE C. & SCRIMGEOUR I. 2004. Thrust tectonic styles of the intracratonic Alice Springs and Petermann Orogenies, central Australia. In: McClay K. R. ed., *Thrust tectonics and hydrocarbon systems: AAPG Memoir 82*, pp 537 - 538.
- FREER R. & EDWARDS A. 1999. An experimental study of Ca-(Fe,Mg) interdiffusion in silicate garnets. *Contributions to Mineralogy and Petrology* **134**, 370-379.
- GANGULY J., CHENG W. & CHAKRABORTY S. 1998. Cation diffusion in aluminosilicate garnets: experimental determination in pyrope-almandine diffusion couples. *Contributions to Mineralogy and Petrology* **131**, 171-180.
- GRAY C. M. & COMPSTON W. 1978. A rubidium-strontium chronology of the metamorphism and prehistory of central Australian granulites. *Geochimica et Cosmochimica Acta* **42**, 1735-1747.
- GREEN E., HOLLAND T. & POWELL R. 2007. An order-disorder model for omphacitic pyroxenes in the system jadeite-diopside-hedenbergite-acmite, with applications to eclogitic rocks. *American Mineralogist* **92**, 1181-1189.
- GREGORY C. J., BUICK I. S., HERMANN J. & RUBATTO D. 2009. Mineral-scale Trace Element and UThPb Age Constraints on Metamorphism and Melting during the Petermann Orogeny (Central Australia). *Journal of Petrology* **50**, 251-287.
- HAND M. & SANDIFORD M. 1999. Intraplate deformation in central Australia, the link between subsidence and fault reactivation. *Tectonophysics* **305**, 121-140.
- HOLLAND T. & POWELL R. 2003. Activity–composition relations for phases in petrological calculations: an asymmetric multicomponent formulation. *Contributions to Mineralogy and Petrology* **145**, 492-501.
- HOLLAND T. J. B. & POWELL R. 1998. An internally consistent thermodynamic data set for phases of petrological interest. *Journal of Metamorphic Geology* **16**, 309-343.
- HOSKINS D. & LEMON N. 1995. Tectonic development of the Eastern Officer Basin, Central Australia. *Exploration Geophysics* **26**, 395-402.
- KELSEY D. E., WHITE R. W. & POWELL R. 2003a. Orthopyroxene–sillimanite–quartz assemblages: distribution, petrology, quantitative P–T–X constraints and P–T paths. *Journal of Metamorphic Geology* **21**, 439-453.
- KELSEY D. E., WHITE R. W., POWELL R., WILSON C. J. L. & QUINN C. D. 2003b. New constraints on metamorphism in the Rauer Group, Prydz Bay, east Antarctica. *Journal of Metamorphic Geology* **21**, 739-759.
- KORSCH R. J., GOLEBY B. R., LEVEN J. H. & DRUMMOND B. J. 1998. Crustal architecture of central Australia based on deep seismic reflection profiling. *Tectonophysics* **288**, 57-69.
- KROHE & WAWRZENITZ 2000. Domainal variations of U–Pb monazite ages and Rb–Sr whole-rock dates in polymetamorphic paragneisses (KTB Drill Core, Germany): influence of strain and deformation mechanisms on isotope systems. *Journal of Metamorphic Geology* **18**, 271-291.
- LEAKE B. E., WOOLLEY A. R., ARPS C. E. S., BIRCH W. D., GILBERT M. C., GRICE J. D., HAWTHORNE F. C., KATO A., KISCH H. J., KRIVOVICHEV V. G., LINTHOUT K., LAIRD J., MANDARINO J. A., MARESCH W. V., NICKEL E. H., ROCK N. M. S., SCHUMACHER J. C., SMITH D. C., STEPHENSON N. C. N., UNGARETTI L., WHITTAKER E. J. W. & GUO YOUZHI 1997. Nomenclature of amphiboles; report of the subcommittee on amphiboles of the International Mineralogical Association, Commission on New Minerals and Mineral Names. *Can Mineral* **35**, 219-246.
- LINDSAY J. F. & LEVEN J. H. 1996. Evolution of a Neoproterozoic to Palaeozoic intracratonic setting, Officer Basin, South Australia. *Basin Research* **8**, 403-424.
- MABOKO M. A. H., MCDUGALL I., ZEITLER P. K. & WILLIAMS I. S. 1992. Geochronological evidence for ~530-550Ma juxtaposition of two Proterozoic metamorphic Terranes in the Musgrave Ranges, central Australia. *Australian Journal of Earth Sciences* **39**, 457-471.

- MABOKO M. A. H., WILLIAMS I. S. & COMPSTON W. 1991. Zircon U-Pb chronometry of the pressure and temperature history of granulites in the Musgrave ranges, central Australia. *Journal of Geology* **99**, 675-697.
- MAJOR R. B. 1973. *Woodroffe, South Australia, 1:250,000 Geological Series*. South Australian Department of Mines and Energy.
- MORIMOTO N. 1988. Nomenclature of Pyroxenes. *Mineralogy and Petrology* **39**, 55-76.
- MORIMOTO N. & KITAMURA M. 1983. Q-J diagram for classification of pyroxenes. *Journal of the Japanese Association of Mineralogy, Petrology and Economic Geology* **78**, 141.
- PAYNE J. L., HAND M., BAROVICH K. M. & WADE B. P. 2008. Temporal constraints on the timing of high-grade metamorphism in the northern Gawler Craton: implications for assembly of the Australian Proterozoic. *Australian Journal of Earth Sciences: An International Geoscience Journal of the Geological Society of Australia* **55**, 623 - 640.
- POWELL R. & HOLLAND T. 1988. An internally consistent dataset with uncertainties and correlations: 3. Applications to geobarometry, worked examples and a computer program. *Journal of Metamorphic Geology* **6**, 173-204.
- POWELL R. & HOLLAND T. 1994. Optimal geothermometry and geobarometry. *American Mineralogist* **79**, 120-133.
- RAIMONDO T., COLLINS A. S., HAND M., WALKER-HALLAM A., SMITHIES R. H., EVINS P. M. & HOWARD H. M. 2009. Ediacaran intracontinental channel flow. *Geology* **37**, 291-294.
- RAIMONDO T., COLLINS A. S., HAND M., WALKER-HALLAM A., SMITHIES R. H., EVINS P. M. & HOWARD H. M. 2010. The anatomy of a deep intracontinental orogen. *Tectonics* **29**, TC4024.
- RAVNA E. J. K., ANDERSEN T. B., JOLIVET L. & DE CAPITANI C. 2010. Cold subduction and the formation of lawsonite eclogite – constraints from prograde evolution of eclogitized pillow lava from Corsica. *Journal of Metamorphic Geology* **28**, 381-395.
- ROBL J., HERGARTEN S., STÜWE K. & HAUZENBERGER C. 2007. THERMAL HISTORY: A new software to interpret diffusive zoning profiles in garnet. *Computers & Geosciences* **33**, 760-772.
- SCHMIDBERGER S. S., SIMONETTI A., HEAMAN L. M., CREASER R. A. & WHITEFORD S. 2007. Lu-Hf, in-situ Sr and Pb isotope and trace element systematics for mantle eclogites from the Diavik diamond mine: Evidence for Paleoproterozoic subduction beneath the Slave craton, Canada. *Earth and Planetary Science Letters* **254**, 55-68.
- SCHWANDT C. S., CYGAN R. T. & WESTRICH H. R. 1996. Ca self-diffusion in grossular garnet. *American Mineralogist* **81**, 448- 451.
- SCRIMGEOUR & CLOSE 1999. Regional high-pressure metamorphism during intracratonic deformation: the Petermann Orogeny, central Australia. *Journal of Metamorphic Geology* **17**, 557-572.
- SMITHIES R. H., HOWARD H. M., EVINS P. M., KIRKLAND C. L., KELSEY D. E., HAND M., WINGATE M. T. D., COLLINS A. S., BELOUSOVA E. & ALLCHURCH S. 2010. Geochemistry, geochronology, and petrogenesis of Mesoproterozoic felsic rocks in the west Musgrave Province, central Australia, and implications for the Mesoproterozoic tectonic evolution of the region. *Geological Survey of Western Australia* **106**.
- SPEAR F. S. 1991. On the interpretation of peak metamorphic temperatures in light of garnet diffusion during cooling. *Journal of Metamorphic Geology* **9**, 379-388.
- SPEAR F. S. 1993. *Metamorphic phase equilibria and pressure-temperature-time paths*. Mineralogical Society of America, Washington.
- STÜWE K. & POWELL R. 1995. PT paths from modal proportions: application to the Koralm Complex, Eastern Alps. *Contributions to Mineralogy and Petrology* **119**, 83-93.
- TATSUMOTO M., KNIGHT R. J. & ALLEGRE C. J. 1973. Time Differences in the Formation of Meteorites as Determined from the Ratio of Lead-207 to Lead-206. *Science* **180**, 1279-1283.
- VAN ACHTERBERGH E., RYAN C. G., JACKSON S. E. & GRIFFIN W. L. 2001. Data reduction software for LA-ICP-MS. In: Paul J. S. ed., *Laser-ablation-ICPMS in earth sciences; principles and applications*, Mineralogical Association of Canada, Ottawa.

- WADE B. P., BAROVICH K. M., HAND M., SCRIMGEOUR I. R. & CLOSE D. F. 2006. Evidence for Early Mesoproterozoic Arc Magmatism in the Musgrave Block, Central Australia: Implications for Proterozoic Crustal Growth and Tectonic Reconstructions of Australia. *Journal of Geology* **114**, 43-63.
- WADE B. P., HAND M. & BAROVICH K. M. 2005. Nd isotopic and geochemical constraints on provenance of sedimentary rocks in the eastern Officer Basin, Australia: implications for the duration of the intracratonic Petermann Orogeny. *Journal of the Geological Society* **162**, 513-530.
- WADE B. P., KELSEY D. E., HAND M. & BAROVICH K. M. 2008. The Musgrave Province: Stitching north, west and south Australia. *Precambrian Research* **166**, 370-386.
- WALTER M. R., VEEVERS J. J., CALVER C. R. & GREY K. 1995. Neoproterozoic stratigraphy of the Centralian Superbasin, Australia. *Precambrian Research* **73**, 173-195.
- WARREN C. J., BEAUMONT C. & JAMIESON R. A. 2008. Formation and exhumation of ultra-high-pressure rocks during continental collision: Role of detachment in the subduction channel. *Geochem. Geophys. Geosyst.* **9**, Q04019.
- WHITE, POWELL, HOLLAND & WORLEY 2000. The effect of TiO₂ and Fe₂O₃ on metapelitic assemblages at greenschist and amphibolite facies conditions: mineral equilibria calculations in the system K₂O-FeO-MgO-Al₂O₃-SiO₂-H₂O-TiO₂-Fe₂O₃. *Journal of Metamorphic Geology* **18**, 497-511.
- WHITE R. W., CLARKE G. L. & NELSON D. R. 1999. SHRIMP U-Pb zircon dating of Grenville-age events in the western part of the Musgrave Block, central Australia. *Journal of Metamorphic Geology* **17**, 465-481.
- WHITE R. W., POWELL R. & CLARKE G. L. 2002. The interpretation of reaction textures in Fe-rich metapelitic granulites of the Musgrave Block, central Australia: constraints from mineral equilibria calculations in the system K₂O-FeO-MgO-Al₂O₃-SiO₂-H₂O-TiO₂-Fe₂O₃. *Journal of Metamorphic Geology* **20**, 41-55.
- WHITE R. W., POWELL R. & HOLLAND T. J. B. 2007. Progress relating to calculation of partial melting equilibria for metapelites. *Journal of Metamorphic Geology* **25**, 511-527.
- YUND R. & TULLIS J. 1991. Compositional changes of minerals associated with dynamic recrystallization. *Contributions to Mineralogy and Petrology* **108**, 346-355.

10. Figure Captions

Figure 1 – Map of Australia depicting the major blocks and basins and their corresponding ages. The thick black dotted lines show the boundaries of the North Australian, West Australian and Gawler Craton. Modified from Wade *et al.* (2006).

Figure 2 – Map of central Australia depicting the spatial relationship of the Musgrave Inlier with surrounding basins and inliers. Note the fault architecture within the Musgrave Province. WT = Woodroffe Thrust. MF = Mann Fault. DSZ = Davenport Shear Zone. The star represents the location of Amata. Modified from Wade *et al.* (2006).

Figure 3 – Simplified geological map of the Amata region and surrounds. The samples are depicted as yellow dots, with the orange dots represent samples of interest. Modified after Major (1973).

Figure 4 – Photomicrographs of each representative petrological group. (A). Large garnet porphyroclasts wrapped in the foliation, which is defined elongated ilmenite and fine grained quartz clusters, taken in plane polarised light. (B) Image (A) in cross polarised light. (C) Large spherical clinopyroxene grain surrounded by a finer grained matrix, taken in plane polarised light. (D) Image (C) taken in cross polarised light. Note the fine grained garnet in the matrix. (E) Large pink relic pyroxenes are prominent in this group, along with plagioclase grains that are highly replaced by kyanite needles, taken in plane polarised light. (F) Image (E) in crossed polarised light. Note the high birefringent pyroxenes. (G) Green hornblende has inclusions rutile. Garnet grains are present mainly in contact with hornblende grains, taken in plane polarised light. (H) Image (G) taken in cross polarised light. Note the faint multiple twins in the plagioclase grains. (I) Vivid green clinopyroxene coronas surrounding pink orthopyroxene grains. Kyanite replacement is extensive within the plagioclase grains. Taken in plane polarised light. (J) Image (I) taken in cross polarised light. Note the garnet along the top of the image. This defines the foliation.

Figure 5 – Photomicrograph showing the location of T1 and T2 on sample A325-907E. The transects are shown for XCa, XFe, Xalm, Xgrs, Xpy and Xspss, determined using microprobe data.

Figure 6 – Photomicrograph showing the location of all transects obtained and their accompanying diffusion profiles. Al data for values of XCa, XFe, Xalm, Xgrs, Xpy and Xspss were collected using an electron microscope. Please note, the transects and profiles for sample are shown in Fig. 5.

Figure 7 – Q-J diagram representing all orthopyroxene and clinopyroxene analyses. Defined using criteria of Morimoto (1988).

Figure 8 – Back-scattered electron images of representative monazite grains from (a) sample A325-875A; (b) A325-318; (c) A325-507C; (d) A325-917D; (e) A325-882. The displayed ages are $^{207}\text{Pb}/^{206}\text{Pb}$ for ages >1Ga and $^{206}\text{Pb}/^{238}\text{U}$ for ages <1Ga. Spot sizes shown are 8 μm .

Figure 9 - Diagrammatic representations of LA-ICPMS monazite data from sample A325-875A. (a) Tera-Wasserburg concordia plot of all monazite data, anchored to common lead (4550Ma; Tatsumoto *et al.* (1973). Regression line and age estimates shown. (b) $^{206}\text{Pb}/^{238}\text{U}$ weighted average of all monazite analyses.

Figure 10 – Diagrammatic representations of LA-ICPMS monazite data from sample A325-318. (a) Conventional concordia plot of all monazite data. (b) Tera-Wasserburg concordia plot of matrix analyses, anchored to common lead (4550Ma; Tatsumoto *et al.* (1973). Regression line and age estimates shown. (c) $^{206}\text{Pb}/^{238}\text{U}$ weighted averages of matrix analyses, including age estimates. (d) Conventional concordia plot of analyses from monazites within garnet grains, including the regression line and age estimates.

Figure 11 – Diagrammatic representations of LA-ICPMS monazite data from sample A325-507A. (a) Conventional concordia plot of all monazite analyses, showing the regression line and age estimates. The grey ellipse indicates data excluded from the plot in (b) for reason mentioned in the text. (b) Conventional concordia plot of all monazite analyses from within garnet. Also shown are the regression line and age estimates.

Figure 12 – Diagrammatic representations of LA-ICPMS monazite data from sample A325-917D. (a) Conventional concordia plot of all monazite data, showing the regression line and age estimates. (b) Tera-Wasserburg plot of upper cluster of analysis, shown in (a). Anchored to common lead (4550Ma; Tatsumoto *et al.* (1973). Also shown is the regression line and age estimates. (c) $^{207}\text{Pb}/^{206}\text{Pb}$ weighted average of data included in (c). Age estimates are included.

Figure 13 – Diagrammatic representations of LA-ICPMS monazite data from sample A325-882. (a) Conventional concordia plot showing all monazite analyses, including the regression line and age estimates. The grey ellipses are data excluded in plot in (b) for reasons outlined in text. (b) $^{207}\text{Pb}/^{206}\text{Pb}$ weighted average of upper cluster of data from (a). Age estimates are included.

Figure 14 – (a) Calculated P - T pseudosection for sample a325-535A. Petrological observations and calculated isopleths ((b) X_{Ca} of gt, (c) X_{Fe} of gt, (d) X_{Fe} di) define a clock-wise pressure-temperature path, typical of metamorphism associated with orogenesis.

Figure 15 – Location of transects T1 and T2 (top) and diffusion profiles with their corresponding models (bottom). The models were fit using the diffusion modelling code of Robl *et al.* (2007) and the parameters outlined in Table 2.

Figure 16 – Modified after Spear (1991). This figure shows how garnets of a smaller radius will record initial (core) compositions that differ from the cores of larger garnets, despite sharing an identical history (cooling history = 10 °C/Myr, Initial T = 750 °C, End T = 400 °C).

11. List of Tables

Table 1 – Compilation of all LA-ICP-MS monazite age data.

Table 2 – Parameters used for diffusion modelling, using the code of Robl *et al.* (2007), for both T1 and T2 from sample a325-907E.

Table 3 – End-member calculations and mineral chemistry for each representative group.

12. Tables

Table 1 - LA-ICP-MS monazite age data

Sample A325-875A															
Spot	Pb204(cps)	Ratios ($\pm 1\sigma$ error)						Age estimates ($\pm 1\sigma$ error)						Conc. (%)	Eff. Age
		Pb207/Pb206		Pb206/U238		Pb207/U235		Pb207/Pb206		Pb206/U238		Pb207/U235			
11b	0	0.06781	0.00177	0.09879	0.00196	0.92294	0.02649	862.7	53.16	607.3	11.52	663.9	13.99	76.96	607.3
11c	0	0.06625	0.00175	0.09768	0.00195	0.89152	0.02581	814.2	54.18	600.8	11.45	647.2	13.85	79.49	600.8
11d	9	0.06393	0.00185	0.09397	0.00254	0.8284	0.03521	739.3	59.33	579	11.29	612.7	14.16	82.88	579
11e	4	0.06281	0.00183	0.09697	0.00192	0.84016	0.0255	701.8	54.1	596.7	11.33	619.2	13.25	88.23	596.7
11f	12	0.06733	0.00118	0.09672	0.0021	0.89829	0.0224	847.9	54.29	595.2	11.47	650.8	13.95	76.75	595.2
11i	12	0.0634	0.00118	0.09876	0.00213	0.86334	0.02299	721.6	79.95	607.1	10.75	631.9	18.6	87.57	607.1
11j	8	0.0641	0.00245	0.09776	0.00183	0.86397	0.03414	744.9	76.87	601.3	10.55	632.3	18.01	84.88	601.3
11o	14	0.06871	0.00289	0.0972	0.00203	0.92113	0.04291	890.2	73.34	598	10.56	663	18.18	74.48	598
20i	0	0.06512	0.00223	0.0965	0.00176	0.86638	0.03048	778.2	66.4	593.8	10.15	633.6	15.86	81.42	593.8
27aa	0	0.06359	0.00121	0.09762	0.00168	0.85597	0.01884	728.1	39.92	600.5	9.88	627.9	10.31	86.24	600.5
27bb	8	0.06343	0.00149	0.10012	0.00179	0.87548	0.02245	722.7	49.2	615.1	10.51	638.5	12.15	88.35	615.1
34a	17	0.06321	0.00141	0.09809	0.00174	0.85483	0.02096	715.4	46.61	603.2	10.19	627.3	11.47	87.69	603.2
34b	0	0.06661	0.00132	0.09545	0.00166	0.87655	0.01979	825.7	40.69	587.7	9.79	639.1	10.71	77.40	587.7
34d	0	0.06323	0.00116	0.09739	0.00167	0.84896	0.01824	715.9	38.48	599.1	9.82	624.1	10.02	87.18	599.1
4b	2	0.06707	0.00167	0.09821	0.00179	0.90812	0.0242	840	50.93	603.9	10.52	656.1	12.88	78.11	603.9

Sample A325-318															
Spot	Pb204(cps)	Ratios ($\pm 1\sigma$ error)						Age estimates ($\pm 1\sigma$ error)						Conc. (%)	Eff. Age*
		Pb207/Pb206		Pb206/U238		Pb207/U235		Pb207/Pb206		Pb206/U238		Pb207/U235			
69a	20	0.08127	0.00198	0.18882	0.00336	2.11508	0.05433	1227.9	46.99	1115	18.24	1153.7	17.71	94.0	1227.9
69b	12	0.07397	0.00114	0.13961	0.00224	1.42327	0.0265	1040.8	30.85	842.5	12.69	898.7	11.1	86.3	842.5
70a	19	0.08225	0.00209	0.10031	0.0018	1.13655	0.03003	1251.6	48.89	616.2	10.56	770.9	14.27	61.6	616.2
70b	0	0.06756	0.00158	0.09379	0.00162	0.87336	0.02172	855.1	47.69	577.9	9.52	637.4	11.77	74.5	577.9
58a	59	0.07152	0.00177	0.10172	0.00178	1.00324	0.02603	972.4	49.63	624.5	10.44	705.5	13.19	72.6	624.5
27a	17	0.07476	0.00088	0.16307	0.00256	1.68017	0.02722	1061.9	23.62	973.8	14.2	1001	10.31	94.3	973.8
2a	5	0.07961	0.00087	0.19502	0.00305	2.14045	0.03339	1187.3	21.36	1148.5	16.44	1162	10.8	97.9	1187.3
3a	25	0.07416	0.00238	0.1098	0.00212	1.1229	0.03626	1045.7	63.42	671.6	12.29	764.4	17.35	73.1	671.6
69d	18	0.0726	0.00205	0.12449	0.00229	1.24599	0.03625	1002.8	56.08	756.3	13.15	821.6	16.39	81.9	756.3
69e	0	0.0683	0.00177	0.0994	0.00179	0.93626	0.02549	877.8	52.6	610.9	10.49	670.9	13.37	76.4	610.9
69g	0	0.07763	0.00149	0.18035	0.00308	1.93077	0.0419	1137.3	37.62	1068.9	16.81	1091.8	14.52	96.0	1068.9
69h	0	0.08424	0.00247	0.16154	0.00313	1.87639	0.0562	1297.9	55.94	965.3	17.35	1072.8	19.84	82.7	1297.9
70c	9	0.0775	0.00198	0.09954	0.00182	1.06392	0.02857	1134.2	50.02	611.7	10.65	735.8	14.06	64.9	611.7
69i	16	0.07446	0.00227	0.12237	0.00235	1.25643	0.03918	1053.6	60.67	744.2	13.52	826.3	17.63	78.4	744.2
69j	6	0.07345	0.00135	0.12749	0.00216	1.29133	0.02734	1026.4	36.76	773.5	12.34	841.9	12.12	82.0	773.5
69k	20	0.08398	0.00288	0.16945	0.00351	1.96217	0.0673	1292.1	65.33	1009.1	19.33	1102.6	23.07	85.3	1292.1
69l	0	0.06171	0.00177	0.09502	0.00176	0.80905	0.02416	664	60.27	585.2	10.38	601.9	13.56	90.6	585.2
70d	12	0.06591	0.00126	0.10042	0.00171	0.9127	0.01995	803.7	39.55	616.9	10.01	658.5	10.59	81.9	616.9

Sample A325-507A															
Spot	Pb204(cps)	Ratios ($\pm 1\sigma$ error)						Age estimates ($\pm 1\sigma$ error)						Conc. (%)	Eff. Age*
		Pb207/Pb206		Pb206/U238		Pb207/U235		Pb207/Pb206		Pb206/U238		Pb207/U235			
2a	7	0.08092	0.00149	0.18638	0.00273	2.08254	0.04101	1219.5	35.88	1101.7	14.83	1143.1	13.51	93.7	1219.5
9a	23	0.09395	0.00162	0.23285	0.0034	3.01767	0.05603	1507	32.18	1349.4	17.78	1412.1	14.16	93.7	1507
15a	4	0.08346	0.00196	0.19596	0.00305	2.25715	0.05435	1279.9	45.24	1153.6	16.42	1199	16.94	93.7	1279.9
16a	0	0.08161	0.0015	0.20583	0.00302	2.31662	0.04548	1236.2	35.54	1206.6	16.13	1217.4	13.92	98.5	1236.2
17a	0	0.07361	0.00147	0.13378	0.00198	1.35753	0.02864	1030.8	39.72	809.4	11.25	870.8	12.34	84.5	809.4
21a	19	0.07032	0.0034	0.13365	0.00253	1.29591	0.06183	937.7	96.21	808.7	14.4	843.9	27.34	90.0	808.7
22a	9	0.08325	0.0018	0.20394	0.00313	2.34467	0.05289	1274.9	41.78	1196.4	16.78	1225.9	16.06	96.2	1274.9
28a	8	0.51987	0.06172	0.15774	0.01334	11.53386	1.0563	4298.6	164.09	944.2	74.27	2567.3	85.57	59.7	944.2
58a	3	0.08773	0.00131	0.24195	0.00349	2.92729	0.04982	1376.6	28.39	1396.8	18.11	1389	12.88	100.9	1376.6
62b	3	0.09233	0.00197	0.23891	0.00378	3.03919	0.06735	1474	40.01	1381.1	19.65	1417.5	16.93	96.2	1474
70a	0	0.08667	0.00145	0.22489	0.00326	2.68534	0.04902	1353.1	31.87	1307.6	17.17	1324.4	13.5	97.9	1353.1
72a	0	0.07296	0.00257	0.15689	0.00272	1.57736	0.05534	1012.9	69.77	939.5	15.14	961.3	21.8	94.9	939.5
74a	31	0.08357	0.00154	0.21834	0.00321	2.51498	0.04923	1282.3	35.52	1273.1	17	1276.4	14.22	99.5	1282.3
75a	0	0.09018	0.00178	0.23378	0.00356	2.90432	0.05913	1429.3	37.1	1354.3	18.58	1383	15.38	96.8	1429.3
81a	24	0.07125	0.00158	0.13097	0.00197	1.28522	0.02951	964.7	44.66	793.4	11.23	839.2	13.11	87.0	793.4
81b	0	0.07009	0.00145	0.11202	0.00167	1.0814	0.02355	931	41.78	684.5	9.7	744.3	11.49	79.9	684.5

Sample A325-917D															
Spot	Pb204(cps)	Ratios ($\pm 1\sigma$ error)						Age estimates ($\pm 1\sigma$ error)						Conc. (%)	Eff. Age*
		Pb207/Pb206		Pb206/U238		Pb207/U235		Pb207/Pb206		Pb206/U238		Pb207/U235			
10a	5	0.07978	0.00104	0.20454	0.00344	2.2506	0.04036	1191.4	25.46	1199.7	18.39	1197	12.61	100.5	1191.4
19a	15	0.07191	0.00149	0.13366	0.00237	1.32538	0.03107	983.5	41.76	808.7	13.45	856.9	13.57	87.1	808.7
24a	0	0.07268	0.00135	0.16228	0.00283	1.62501	0.03523	1005	37.15	969.4	15.68	979.9	13.63	97.5	969.4
30a	0	0.06598	0.0012	0.11198	0.00194	1.01887	0.02202	805.7	37.65	684.3	11.24	713.3	11.08	88.5	684.3
36a	0	0.0769	0.00102	0.19198	0.00324	2.03524	0.03673	1118.5	26.13	1132.1	17.51	1127.4	12.29	100.8	1118.5
78a	0	0.07853	0.00096	0.205	0.00344	2.21994	0.03877	1160.3	24.13	1202.1	18.41	1187.4	12.23	102.3	1160.3
79a	7	0.0725	0.00096	0.13977	0.00237	1.39728	0.02535	1000	26.62	843.4	13.39	887.8	10.74	88.8	843.4
79b	12	0.07287	0.00148	0.1239	0.00221	1.24448	0.02877	1010.4	40.62	753	12.66	820.9	13.02	81.2	753
88a	22	0.0781	0.00138	0.19156	0.00338	2.06257	0.04373	1149.5	34.66	1129.8	18.26	1136.5	14.5	98.9	1149.5
10b	8	0.0823	0.00112	0.20482	0.0035	2.32205	0.04303	1252.6	26.26	1201.1	18.73	1219	13.15	97.3	1252.6
19b	4	0.06769	0.00153	0.12618	0.00228	1.17616	0.02942	859.1	46.15	766	13.04	789.5	13.73	91.9	766
30b	8	0.07139	0.00134	0.14553	0.00257	1.43049	0.03163	968.6	37.78	875.8	14.49	901.8	13.22	93.1	875.8
78b	4	0.07987	0.00096	0.2063	0.00348	2.26974	0.03983	1193.9	23.61	1209.1	18.61	1202.9	12.37	100.8	1193.9
88b	3	0.07866	0.00122	0.17899	0.0031	1.93945	0.03828	1163.5	30.33	1061.5	16.94	1094.8	13.22	94.1	1163.5
19c	0	0.07683	0.00167	0.14225	0.00258	1.50509	0.0366	1116.7	42.75	857.4	14.55	932.5	14.84	83.5	857.4
79d	7	0.08059	0.0012	0.19142	0.00329	2.12568	0.04108	1211.5	28.94	1129	17.79	1157.2	13.34	95.5	1211.5

Sample A325-882															
Spot	Pb204(cps)	Ratios ($\pm 1\sigma$ error)						Age estimates ($\pm 1\sigma$ error)						Conc. (%)	Eff. Age
		Pb207/Pb206		Pb206/U238		Pb207/U235		Pb207/Pb206		Pb206/U238		Pb207/U235			
60a	12	0.07251	0.00176	0.1514	0.00262	1.51297	0.03852	1000.3	48.55	908.8	14.66	935.6	15.56	93.5	908.8
61a	7	0.07505	0.00136	0.18328	0.00297	1.89648	0.03851	1069.9	35.89	1084.9	16.16	1079.9	13.5	100.9	1084.9
61b	11	0.06124	0.00171	0.09794	0.00172	0.82626	0.02376	647.6	59.01	602.3	10.13	611.5	13.21	94.4	602.3
62a	38	0.07689	0.00181	0.20112	0.00347	2.1307	0.053	1118.2	46.39	1181.3	18.63	1158.8	17.19	103.6	1118.2
62b	27	0.06762	0.00158	0.10686	0.00181	0.9966	0.02456	857	47.72	654.5	10.53	702.1	12.49	81.9	654.5
63a	2	0.05756	0.0022	0.09696	0.0019	0.76869	0.02916	512.8	81.81	596.6	11.15	579	16.74	112.9	596.6
3a	0	0.08051	0.00222	0.20747	0.0038	2.30144	0.06479	1209.6	53.42	1215.3	20.28	1212.7	19.93	100.3	1209.6
4a	3	0.07789	0.00158	0.20972	0.0035	2.25138	0.0498	1144	39.69	1227.3	18.64	1197.2	15.55	104.7	1144
16a	0	0.07599	0.00145	0.21047	0.00348	2.20237	0.04665	1094.8	37.72	1231.3	18.53	1181.8	14.79	107.9	1094.8
30a	0	0.06599	0.00168	0.1225	0.00214	1.11298	0.02945	806.1	52.32	744.9	12.28	759.6	14.15	94.2	744.9
10a	15	0.07932	0.00168	0.19093	0.00318	2.08802	0.04775	1180.2	41.29	1126.4	17.22	1144.9	15.7	97.0	1126.4
15a	0	0.07003	0.00195	0.15629	0.00279	1.50818	0.04309	929.2	56.09	936.1	15.54	933.7	17.45	100.5	936.1
20a	2	0.07846	0.00173	0.20908	0.00352	2.2599	0.05328	1158.6	43.02	1223.9	18.77	1199.9	16.6	103.6	1158.6
32a	9	0.07811	0.00145	0.19359	0.00314	2.08316	0.04339	1149.7	36.47	1140.8	16.95	1143.3	14.29	99.4	1149.7
54a	4	0.0806	0.00133	0.20828	0.0033	2.31189	0.04428	1211.6	32.07	1219.7	17.58	1215.9	13.57	100.4	1211.6
62c	0	0.06998	0.00143	0.1491	0.00242	1.43825	0.03201	927.8	41.29	895.9	13.59	905	13.33	97.5	895.9
32b	33	0.08078	0.00137	0.20614	0.00328	2.29333	0.04485	1216.1	33.04	1208.2	17.54	1210.2	13.83	99.5	1216.1
62d	19	0.07733	0.00146	0.18991	0.00306	2.02232	0.0426	1129.7	37.23	1120.9	16.59	1123	14.31	99.4	1129.7
30b	8	0.07217	0.00262	0.10371	0.00204	1.03068	0.03706	990.7	72.06	636.1	11.89	719.3	18.53	72.6	636.1

*For ages <1000 Ma and >1000 Ma, effective age corresponds to calculated 206Pb/238U and 207Pb/206Pb ages, respectively.

*Spots highlighted by an asterisk indicate analyses not used in final results. See text for details.

Table 2 - Diffusion modelling parameters

	Transect 1	Transect 2
Radius (μm)	127.7	61.7
XCa Plagioclase	0.94	0.94
VBt	0.9	0.9
VGt	0.1	0.1
$D_0\text{Fe}$ (m^2/s)	3.50E-09	3.50E-09
QFe (J/mol)	274186	274186
$D_0\text{Ca}$ (m^2/s)	1.22E-06	1.22E-06
QCa (J/mol)	236801	236801
Start Temp. (K)	353.15	353.15
End Temp. (K)	923.15	923.15
Duration (Myr)	0.1	27

Table 3 - Summary of mineral chemistry from all defined petrological groups

	Felsic Mylonites	Dolerite dykes	Hornblende- bearing mylonites	Coronitic clinopyroxene- bearing mylonites	Mafic mylonites
<i>New garnet</i>					
X(alm)	0.457	0.502	0.567	0.496	0.631
X(py)	0.199	0.242	0.174	0.219	0.143
X(grs)	0.327	0.245	0.247	0.261	0.191
X(spss)	0.017	0.011	0.012	0.024	0.035
<i>Old garnet</i>					
X(alm)	0.517	n/a	0.580	-	-
X(py)	0.394	n/a	0.144	-	-
X(grs)	0.065	n/a	0.263	-	-
X(spss)	0.025	n/a	0.013	-	-
<i>New Clinopyroxene</i>					
XCa	-	0.458	0.454	0.418	-
XFe	-	0.140	0.167	0.153	-
XMg	-	0.402	0.379	0.429	-
XNa	-	0.227	0.153	0.187	-
<i>Old Clinopyroxene</i>					
XCa	-	0.459	0.444	0.448	0.456
XFe	-	0.138	0.171	0.192	0.160
XMg	-	0.403	0.384	0.360	0.384
XNa	-	0.204	0.184	0.193	0.104
<i>Orthopyroxene</i>					
XCa	-	-	-	0.161	0.018
XFe	-	-	-	0.301	0.476
XMg	-	-	-	0.539	0.506
<i>Biotite</i>					
TiO ₂ (wt%)	-	5.522	-	3.717	4.189
XMg	-	0.656	-	0.726	0.693
XFe	-	0.344	-	0.274	0.307
<i>Hornblende</i>					
XFe	-	-	0.435	-	-
XMg	-	-	0.565	-	-
<i>Plagioclase</i>					
XNa	0.666	0.831	0.931	0.643	0.549
XCa	0.267	0.169	0.069	0.357	0.438
XK	0.067	-	-	-	0.013
<i>K-Feldspar</i>					
XK	0.748	-	-	0.923	0.895
XNa	0.191	-	-	0.077	0.100
XCa	0.061	-	-	-	0.005
<i>Ilmenite</i>					
Xilm	0.728	n/a	0.999	0.654	0.923
XFe	0.669	n/a	0.513	0.622	0.519
XTi	0.331	n/a	0.487	0.378	0.481
XMn	0.004	n/a	0.004	0.003	0.011
<i>Magnetite</i>					
XAl	-	-	-	0.007	0.005
TiO ₂ (wt%)	-	-	-	0.087	0.084

*n/a denotes no analyses were taken for this mineral within this group

* - denotes this mineral does not exist for this group

13. Figures

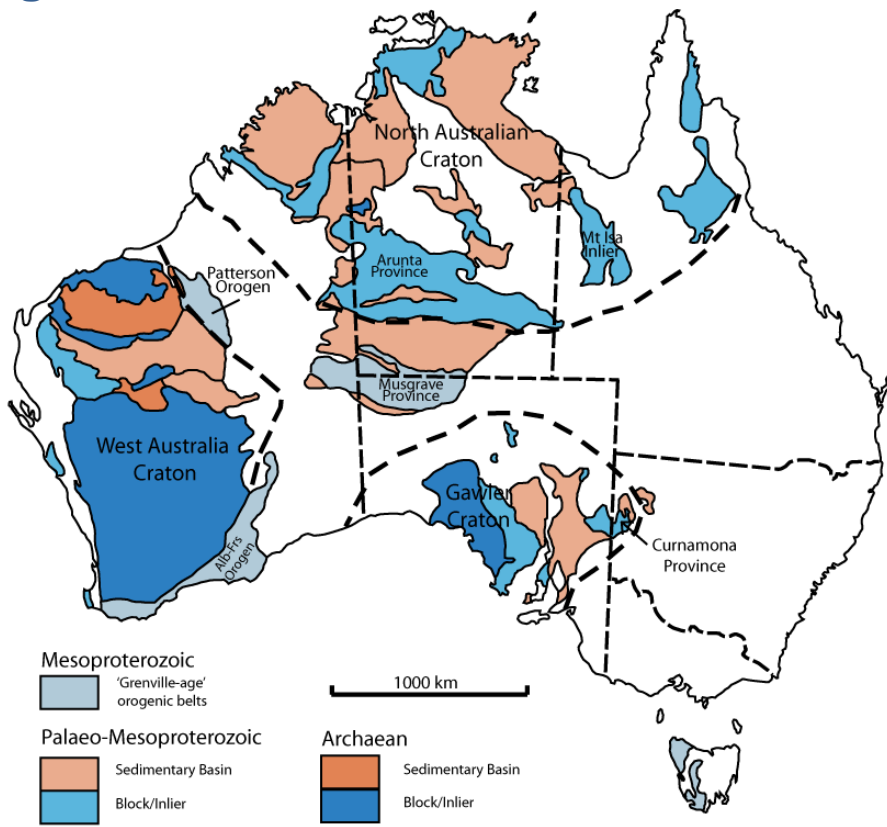


Figure 1

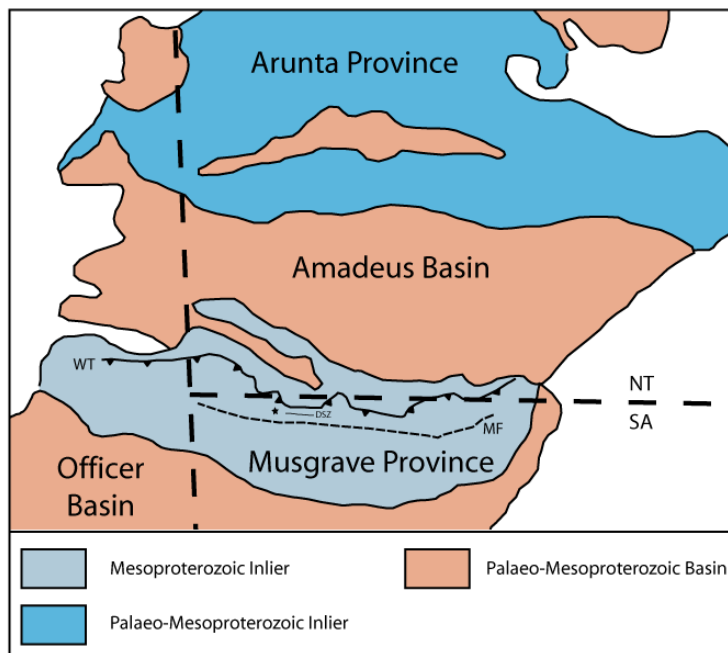
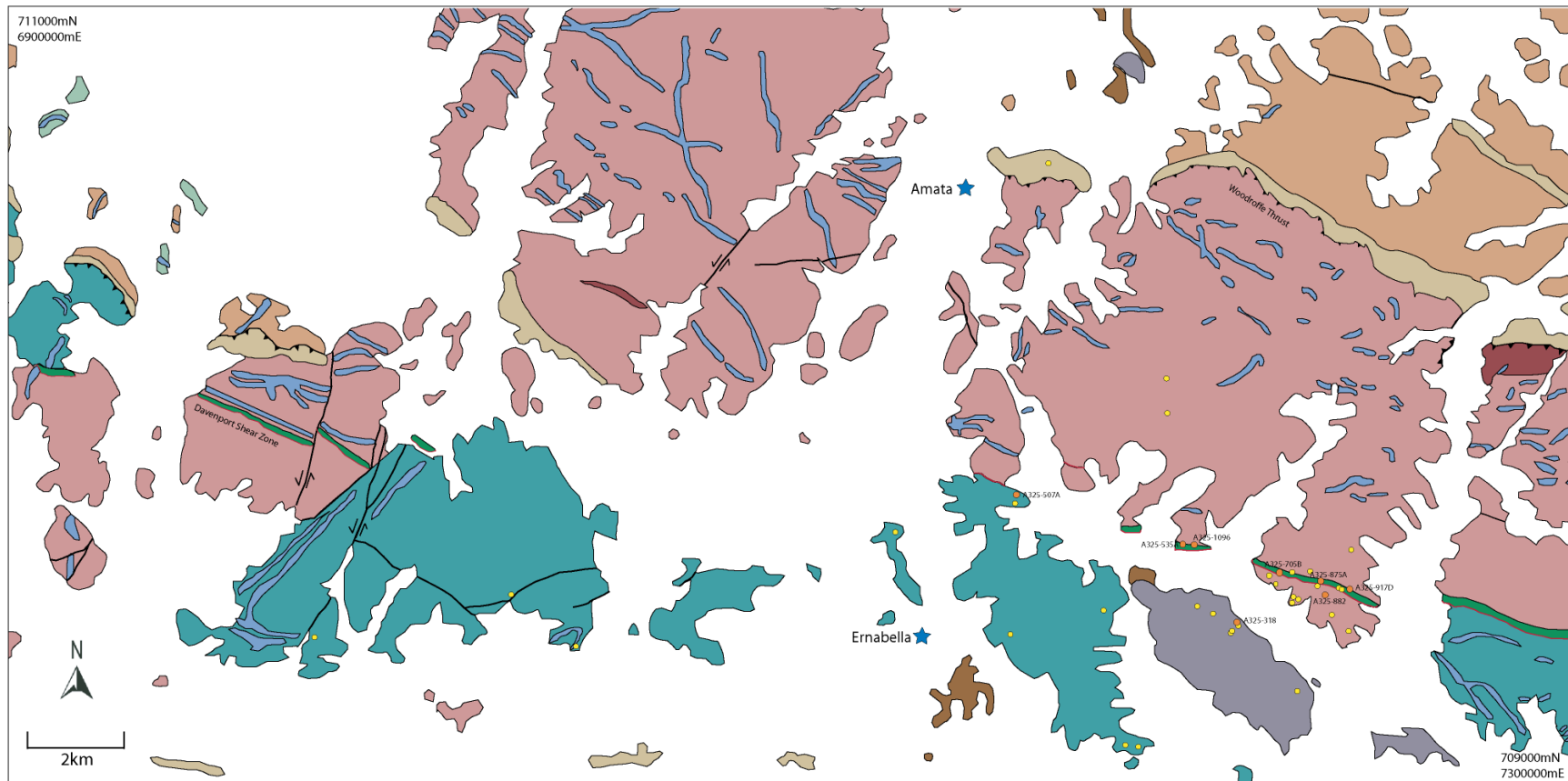


Figure 2



- Mesoproterozoic**
- Altered basic dyke in shear zones, e.g. Davenport shear zone.
 - Dolerite and gabbro dykes.
 - Norites, gabbros, anorthosites and troctolites.
 - Pitjantjatjara Supersuite: Adamellite; alkali granite; diorite.
 - Gneissic granite
 - Birksgate Complex: Gneiss, granulite and amphibolite facies.
 - Altered granulite and gneissic granulite (structurally above the Woodroffe Thrust).

- Palaeoproterozoic**
- Olla Gneiss: Gneiss, with minor schist, amphibolite and quartzite
 - Altered granulite and gneissic granulite (structurally below the Woodroffe Thrust).
- Miscellaneous**
- Mylonites and cataclasites including the Woodroffe Thrust
-
- Sample of interest
 - Sample location
 - Locality
 - Fault - observed
 - Davenport Shear Zone
 - Fault - thrust

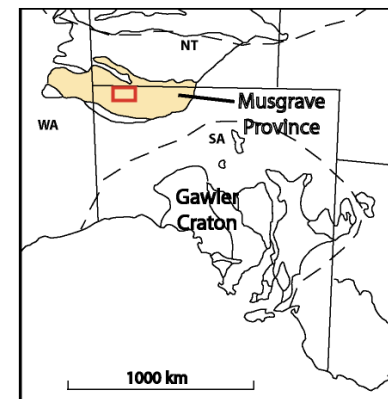


Figure 3

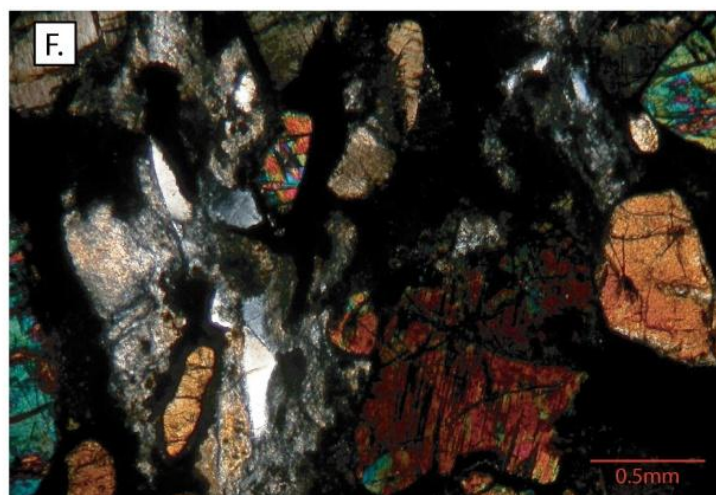
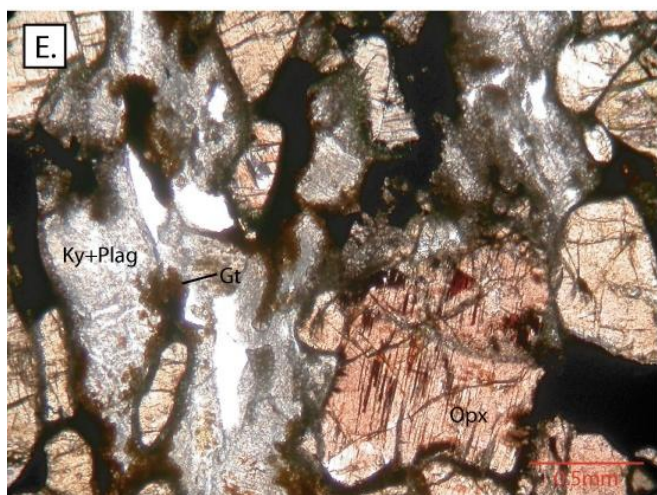
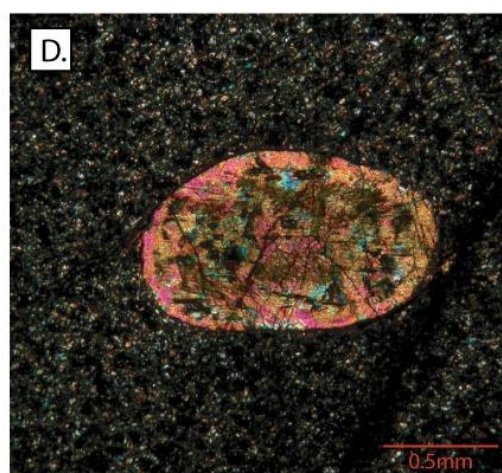
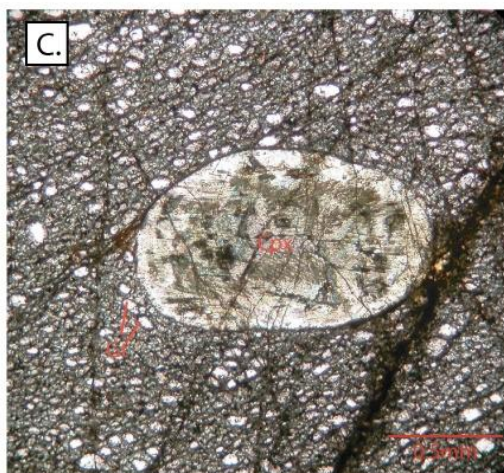
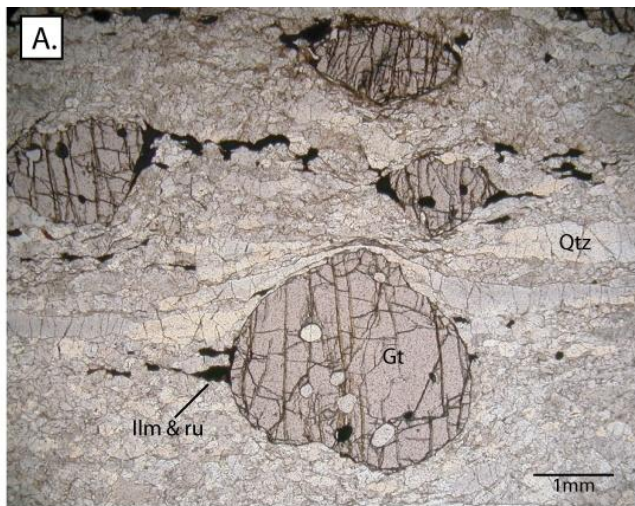


Figure 4

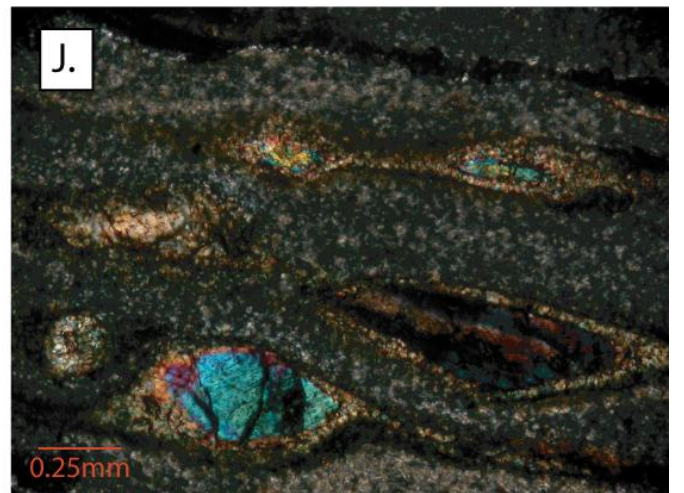
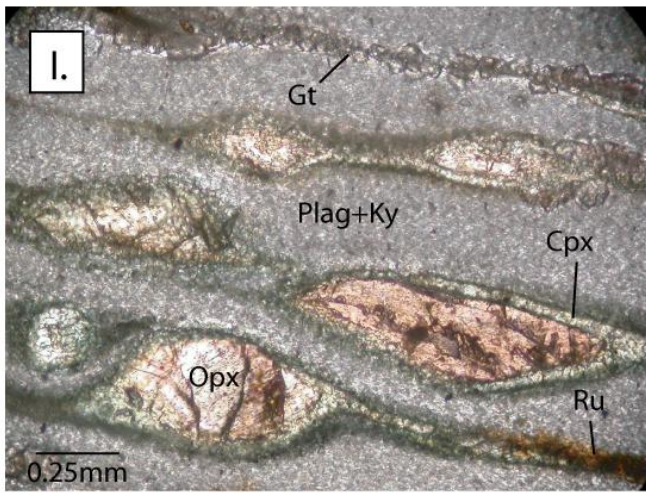
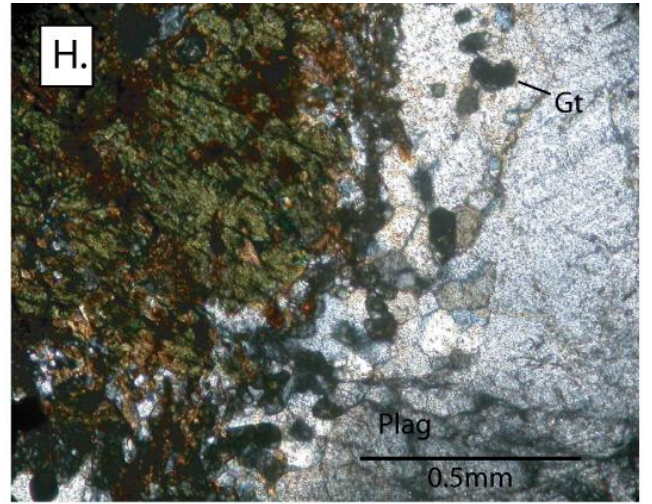
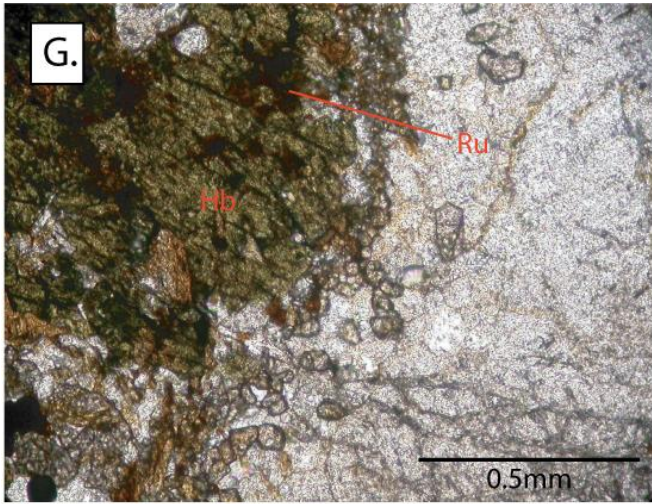


Figure 4

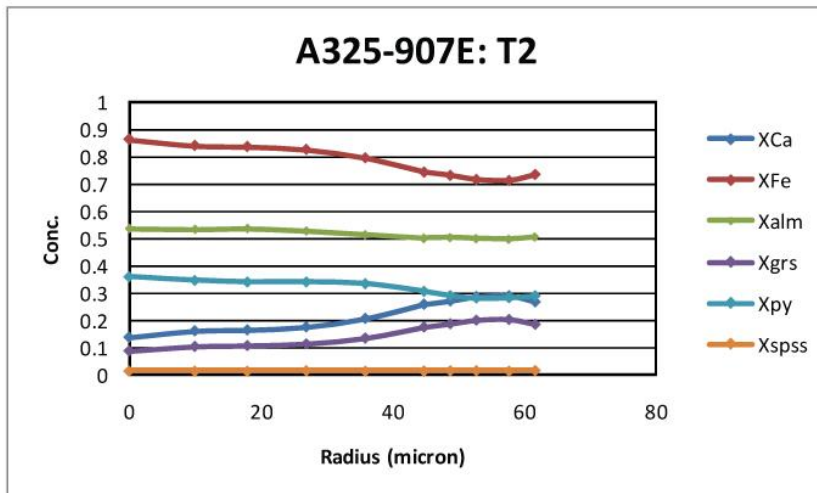
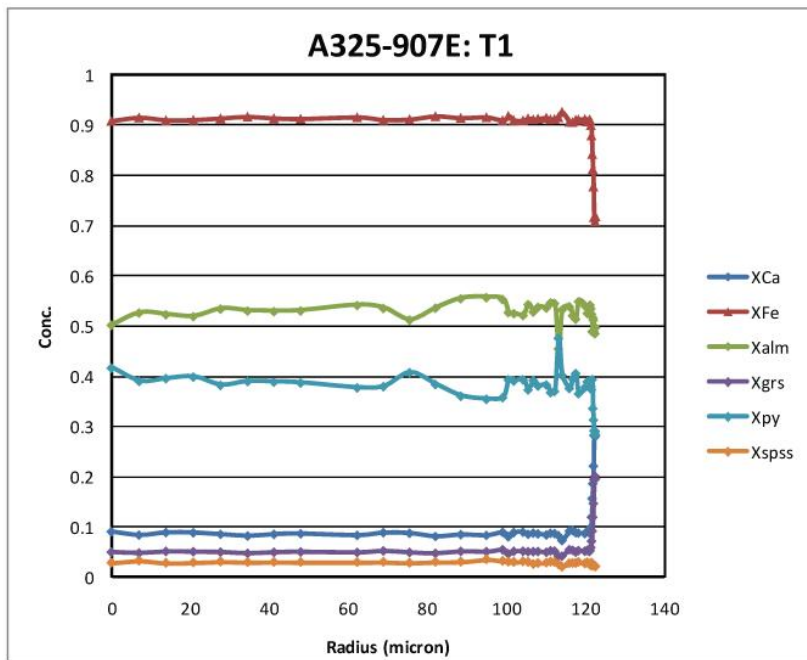
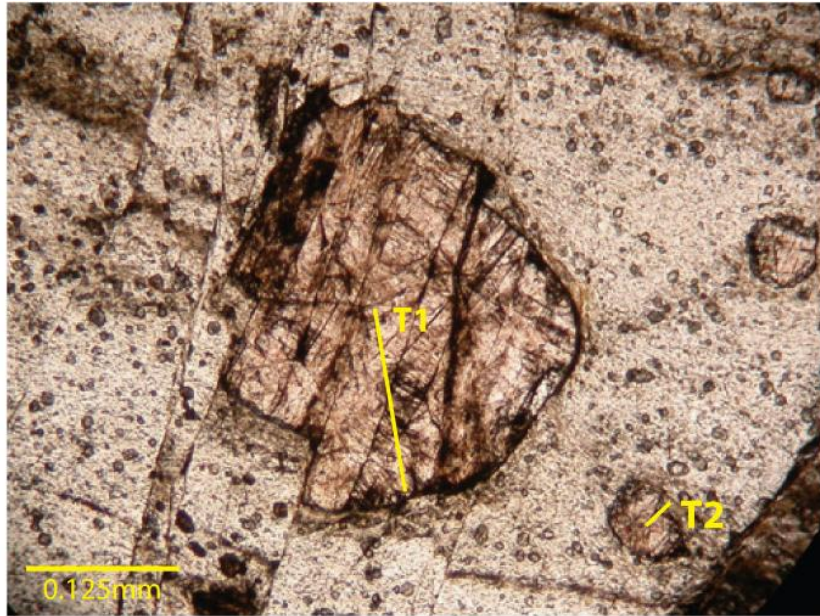


Figure 5

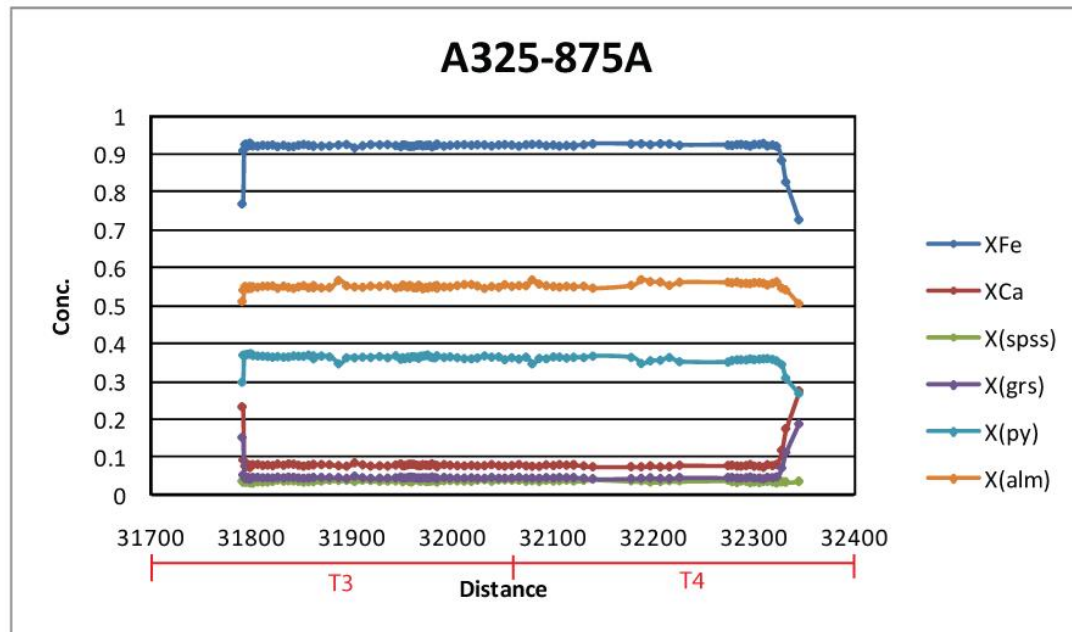
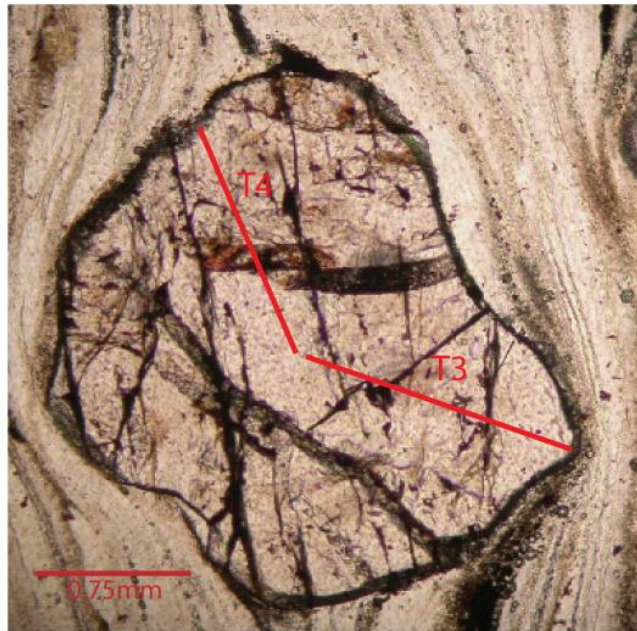
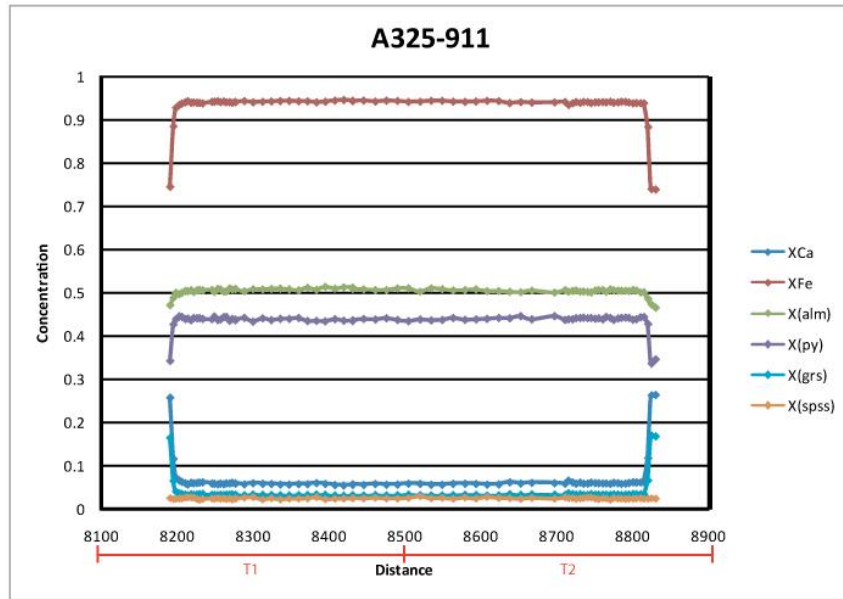
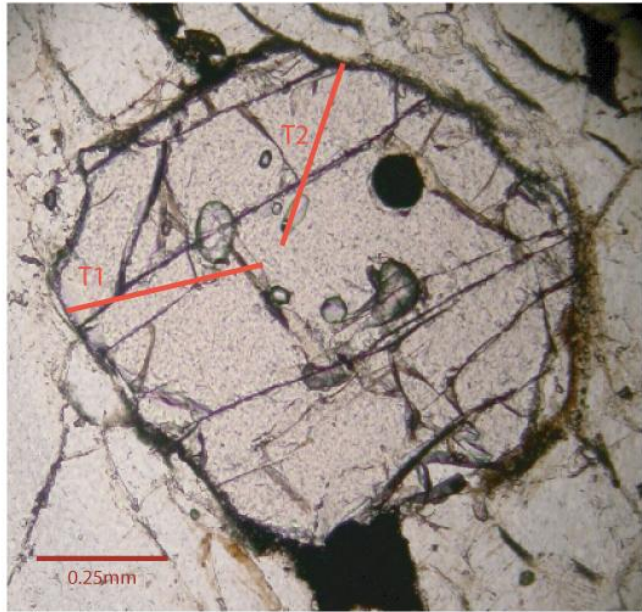


Figure 6

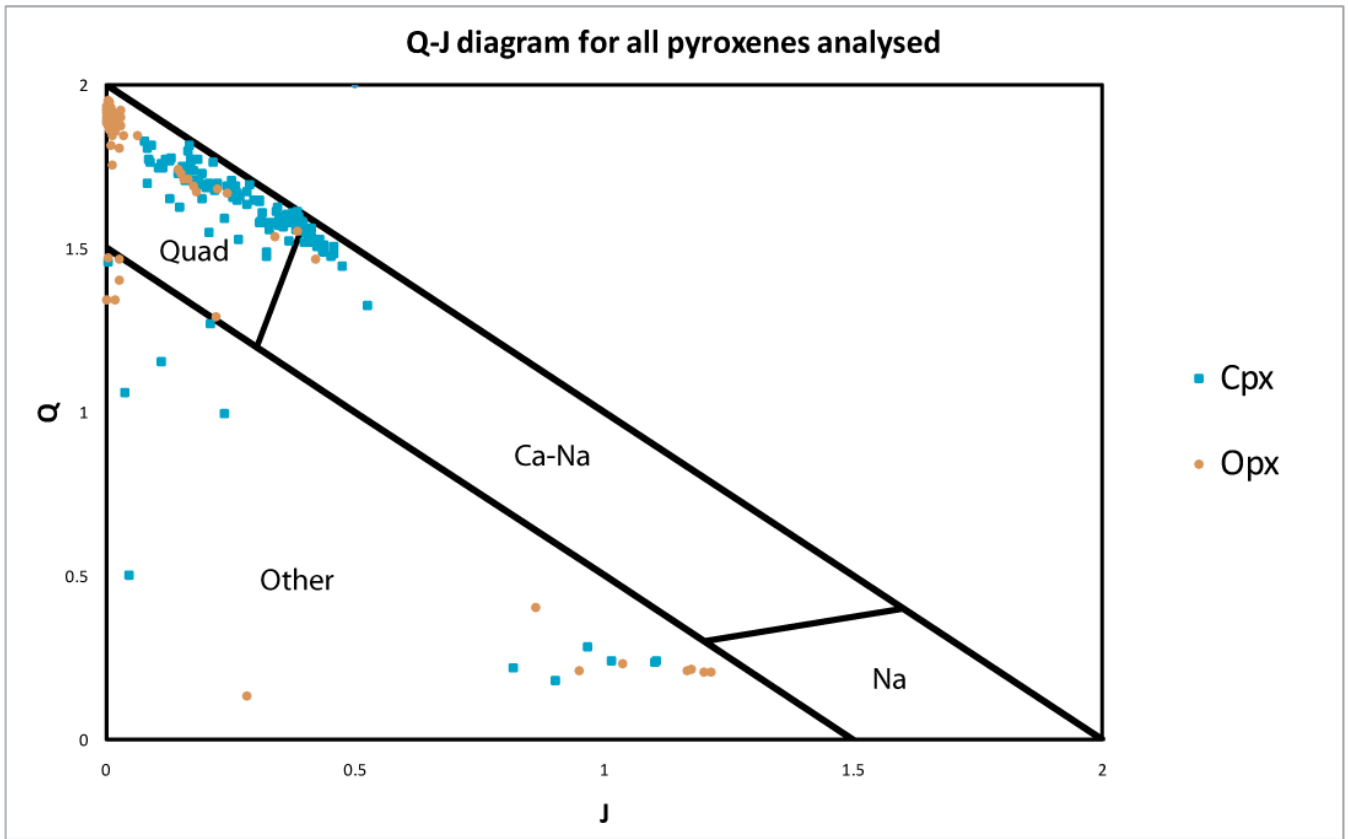
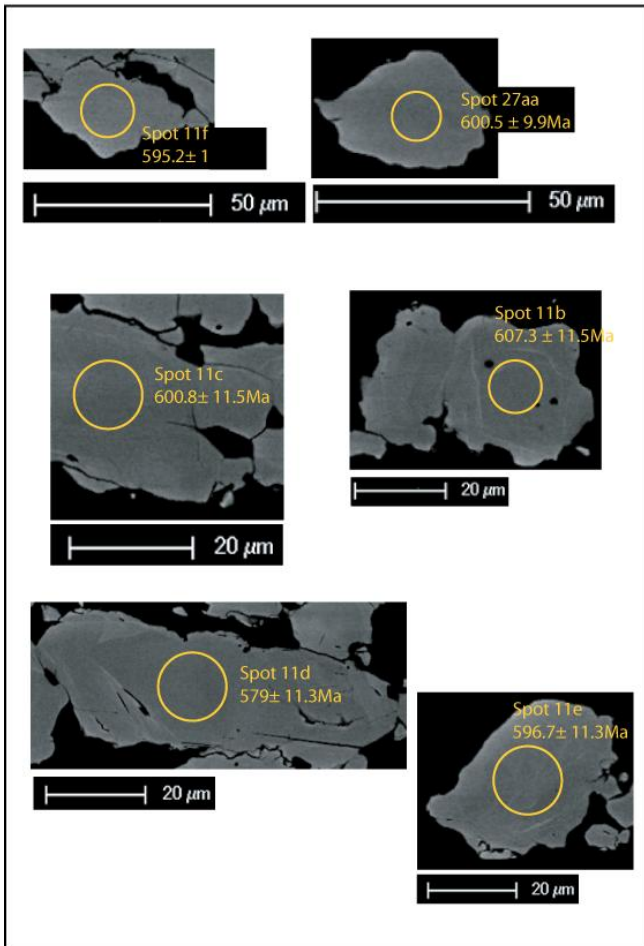
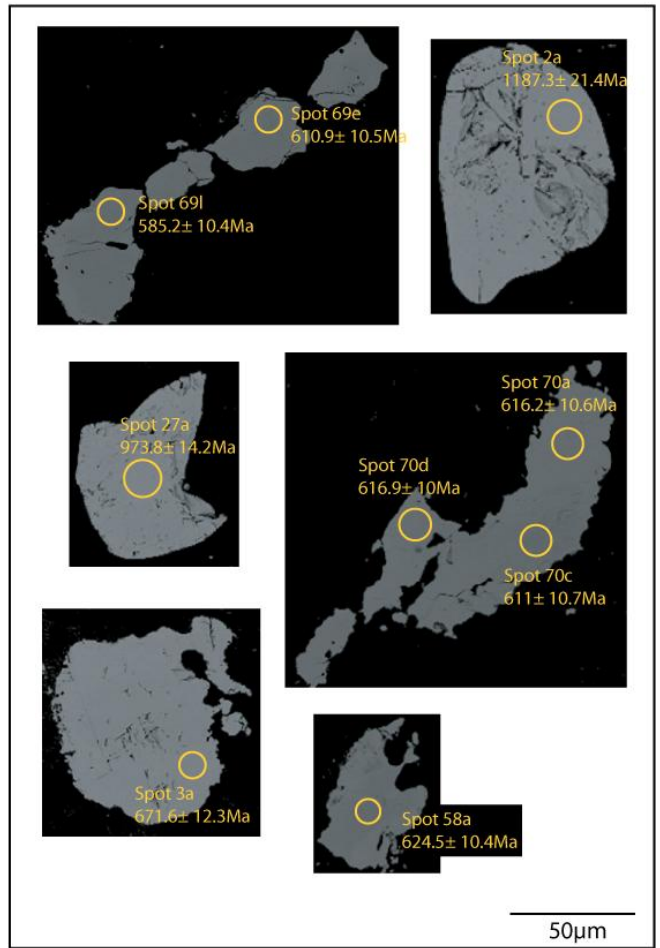


Figure 7

(a) Sample A325-875A



(b) Sample A325-318



(c) Sample A325-507C

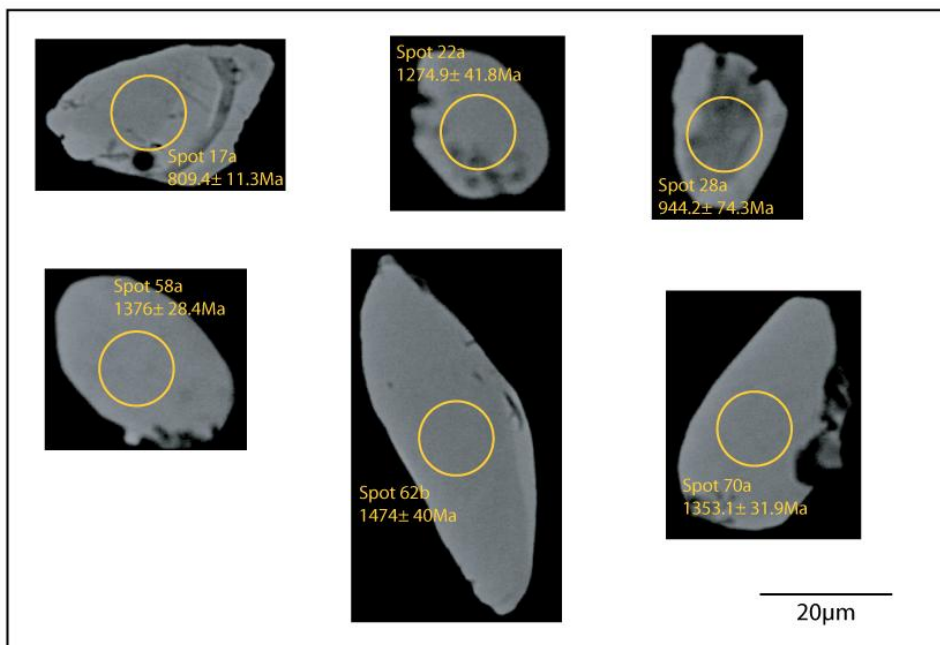
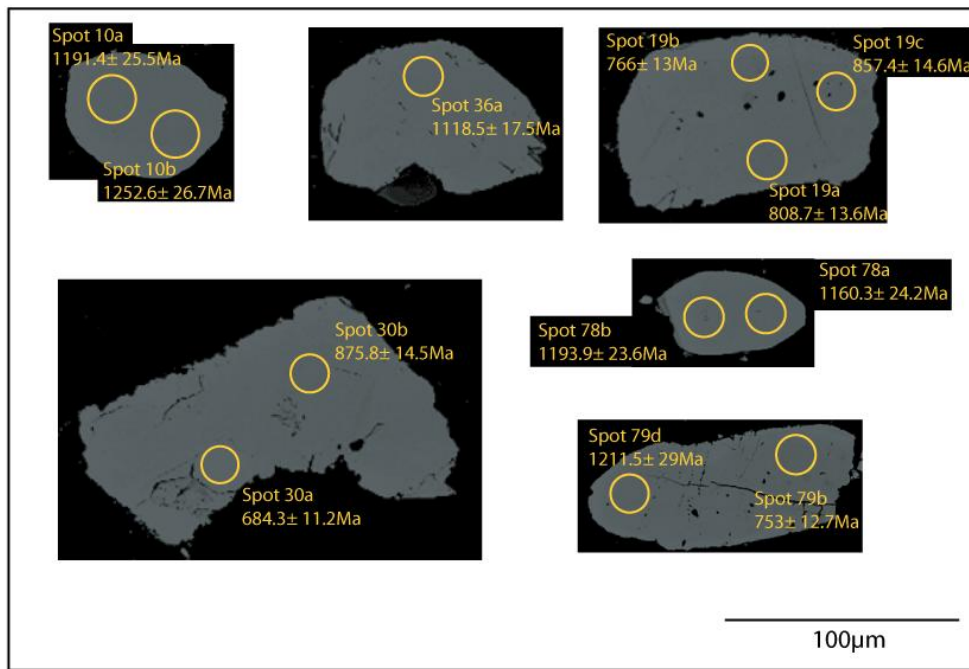


Figure 8

(d) Sample A325-917D



(e) Sample A325-882

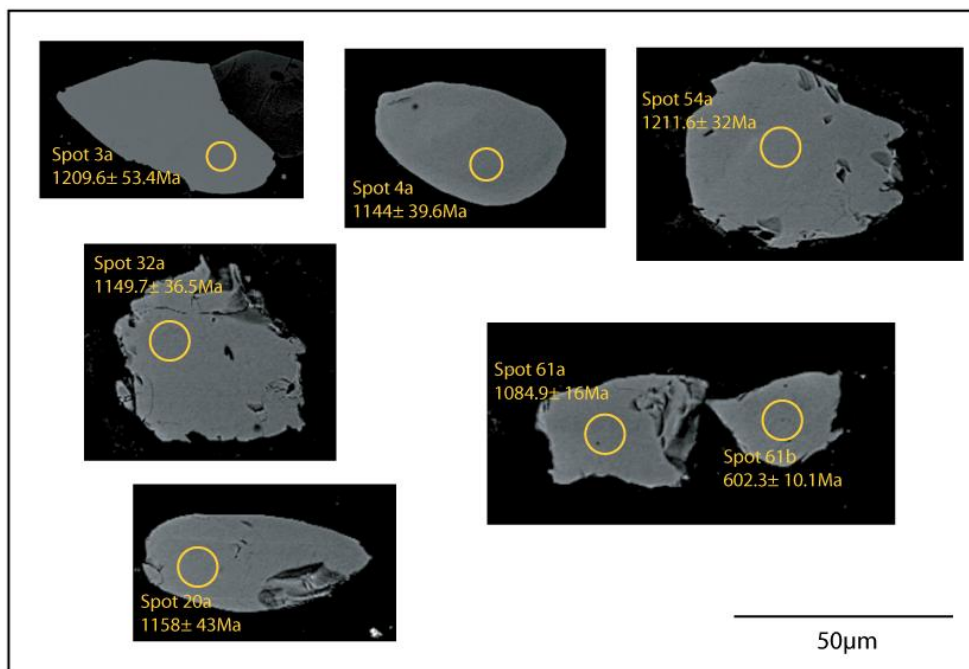
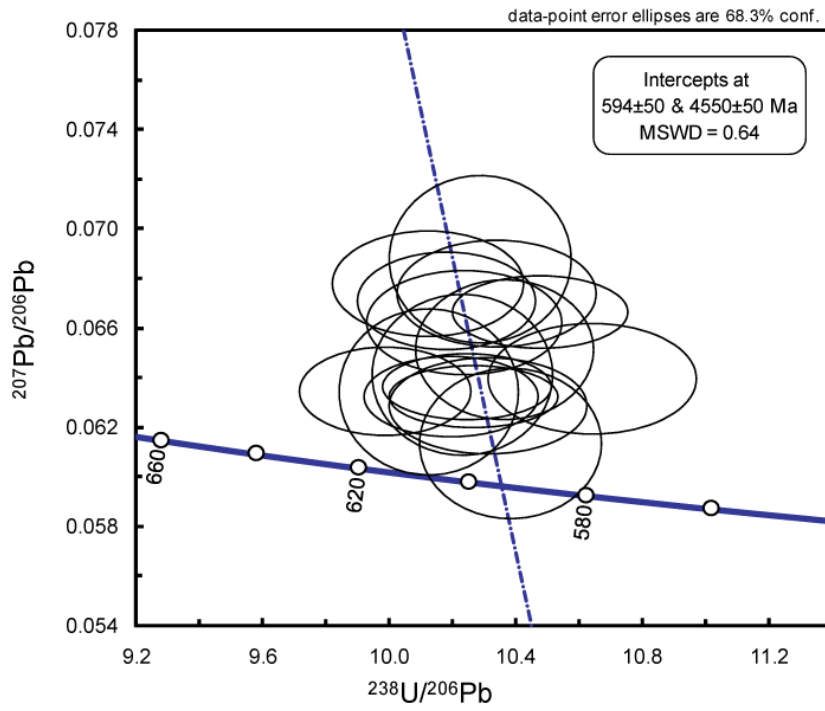


Figure 8

Sample A325-875A

(a) All data



(b) $^{238}\text{U}/^{206}\text{Pb}$ weighted average

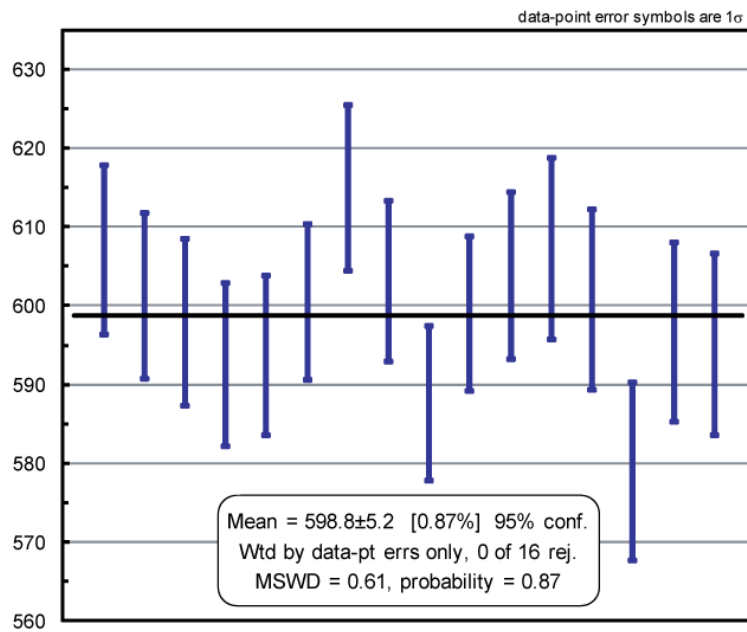
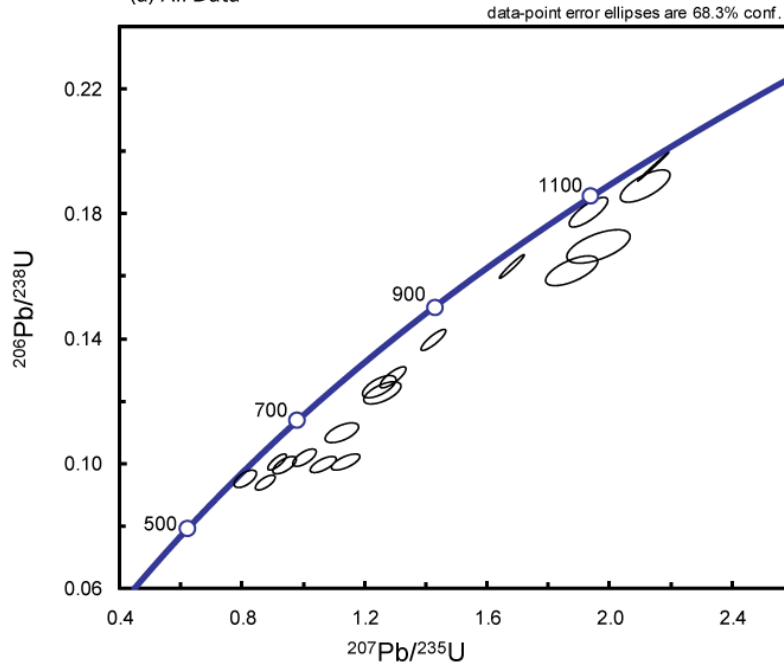


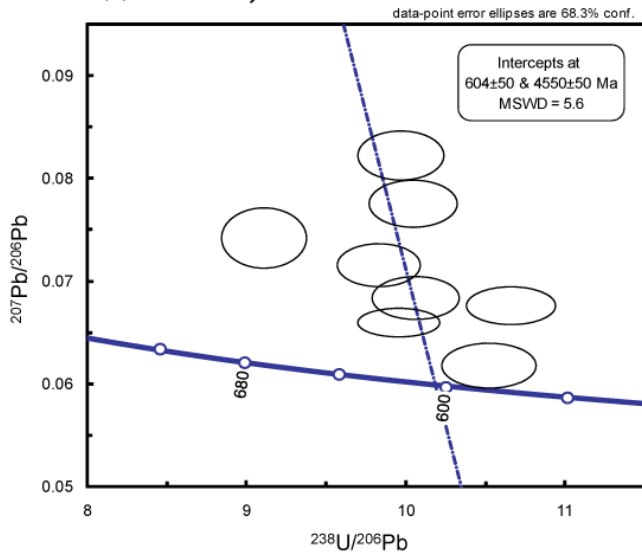
Figure 9

Sample A325-318

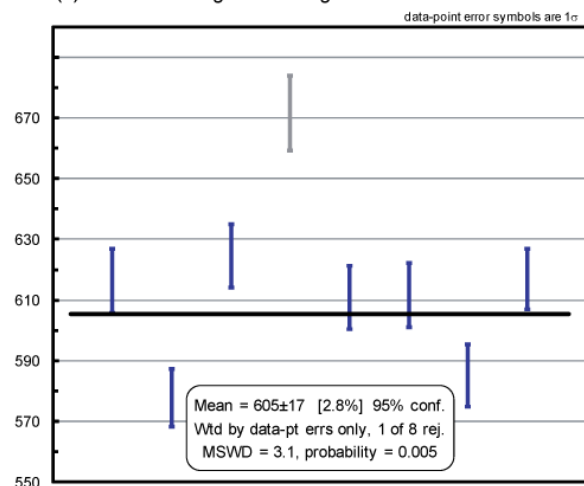
(a) All Data



(b) Matrix analyses



(c) $^{238}\text{U}/^{206}\text{Pb}$ weighted average



(d) Garnet analyses

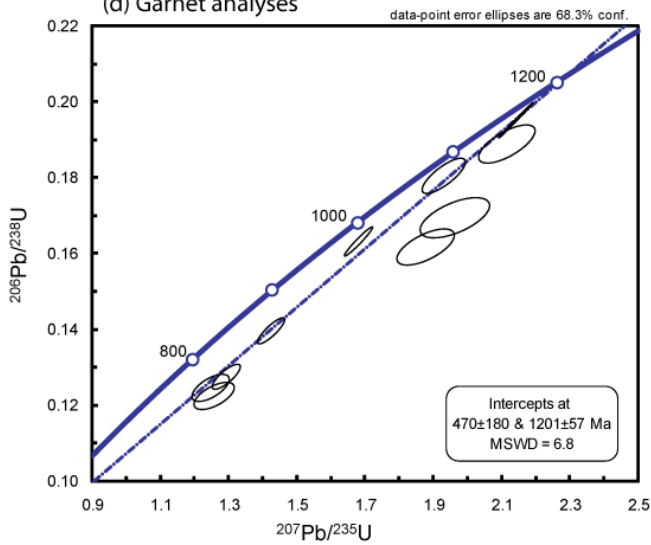


Figure 10

A325-507A

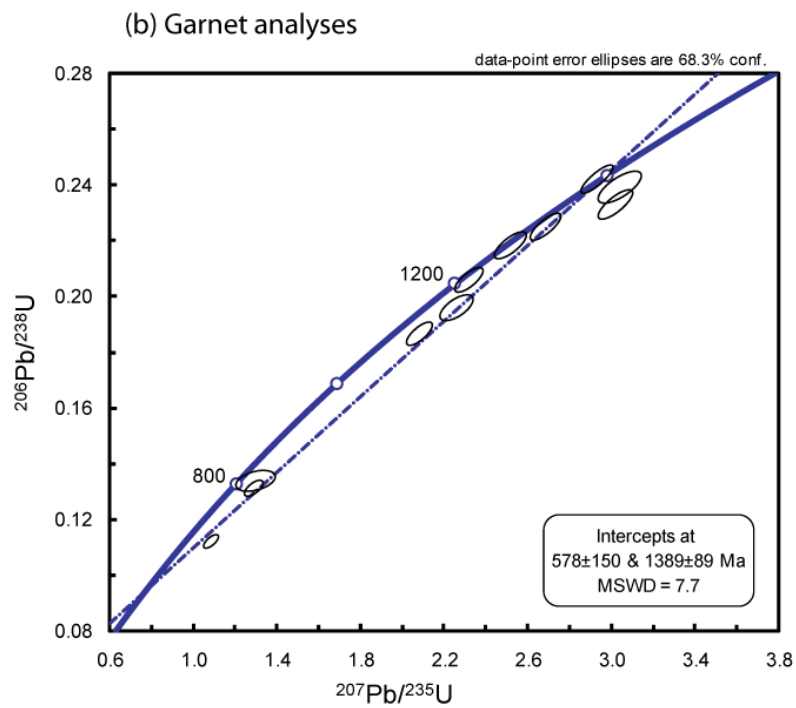
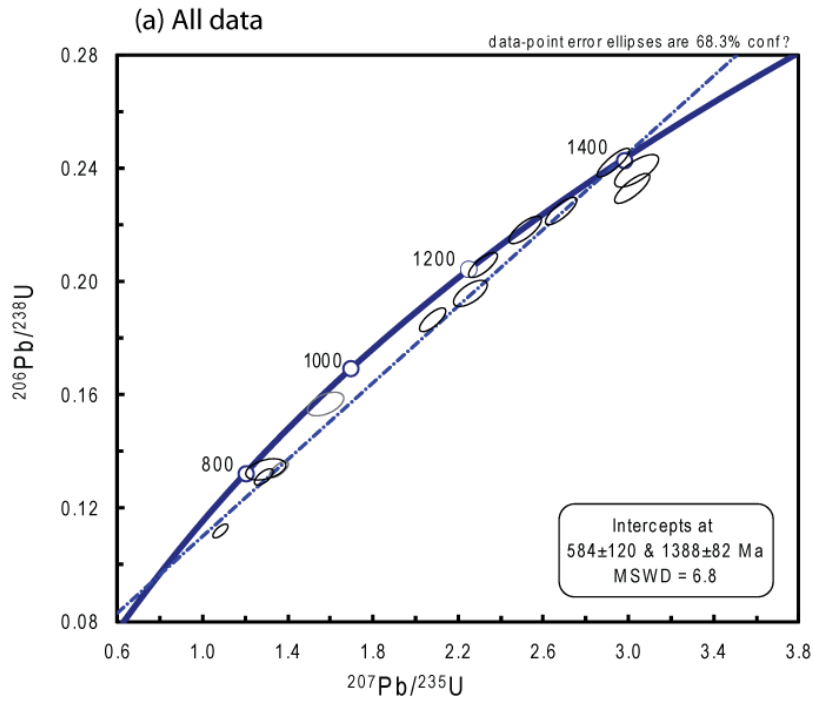


Figure 11

Sample A325-917D

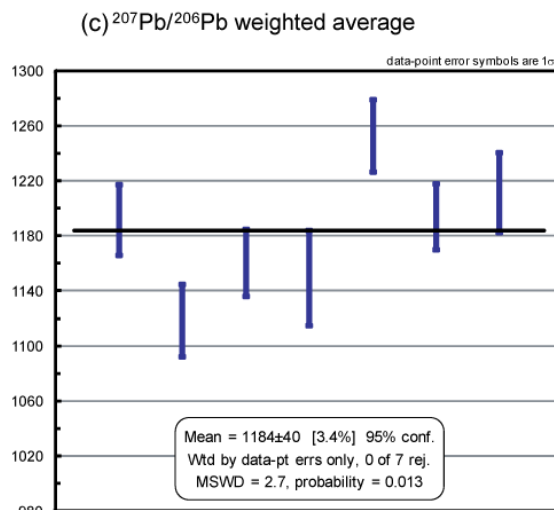
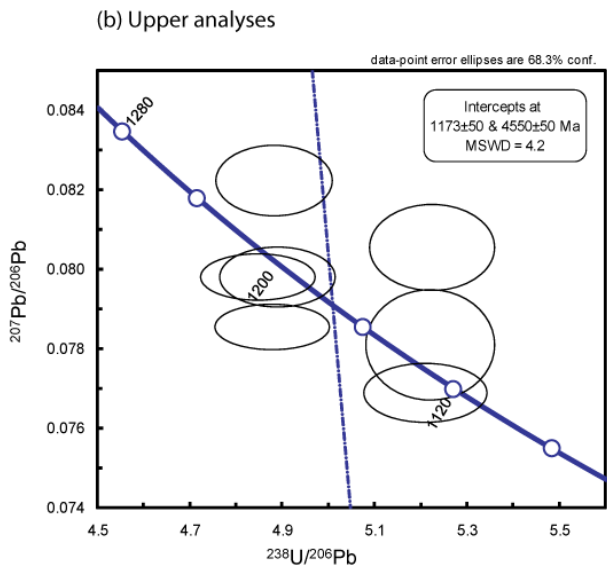
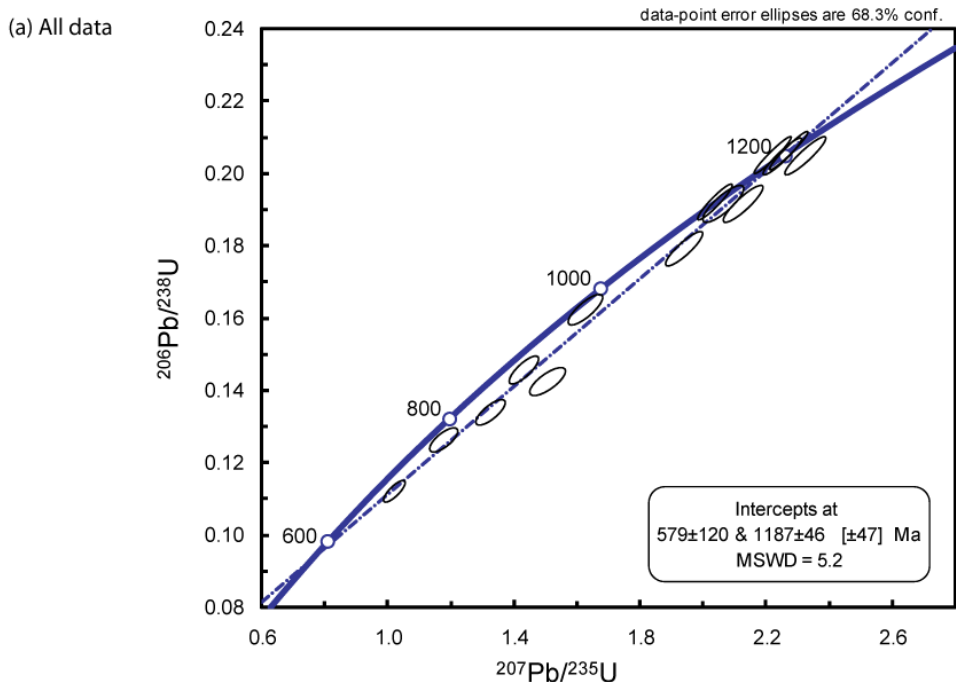


Figure 12

A325-882

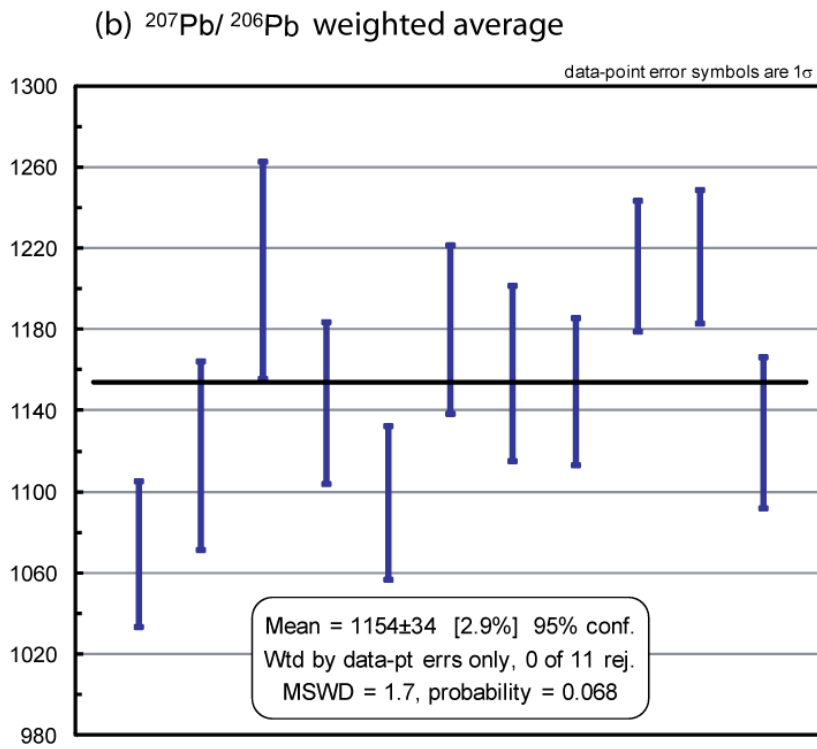
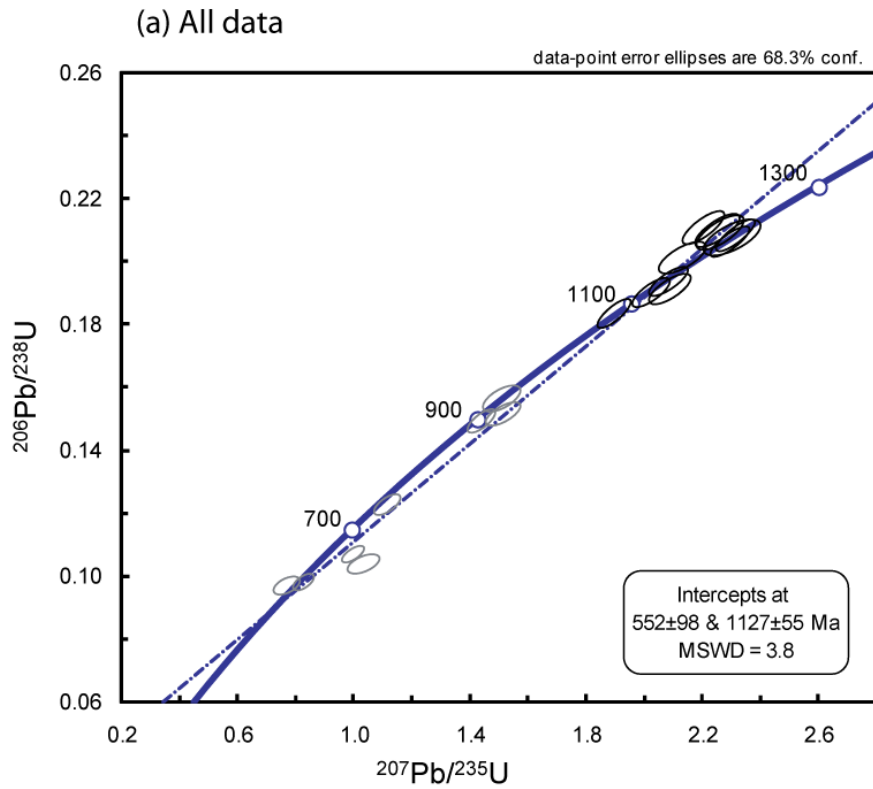


Figure 13

(a) Calculated pseudosection for sample A325-535A

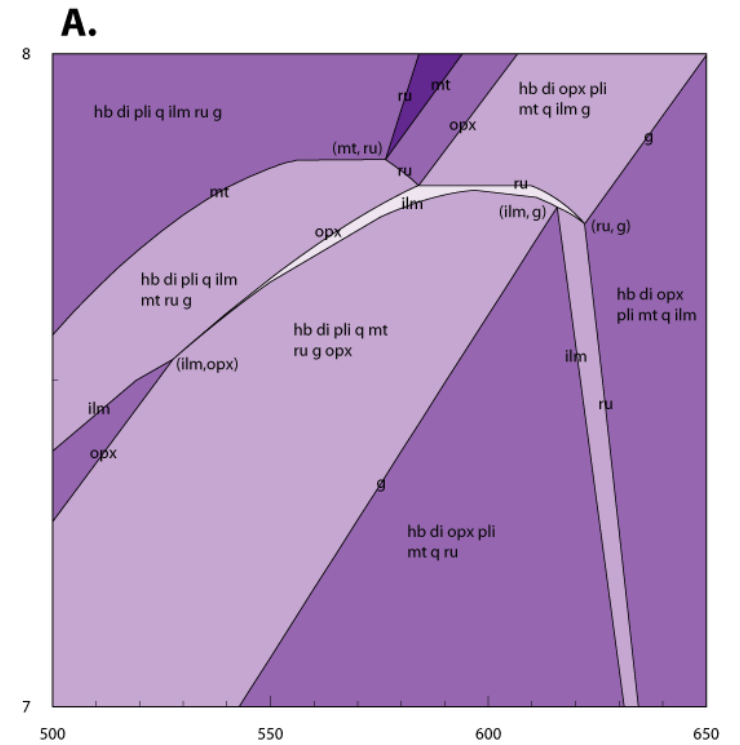
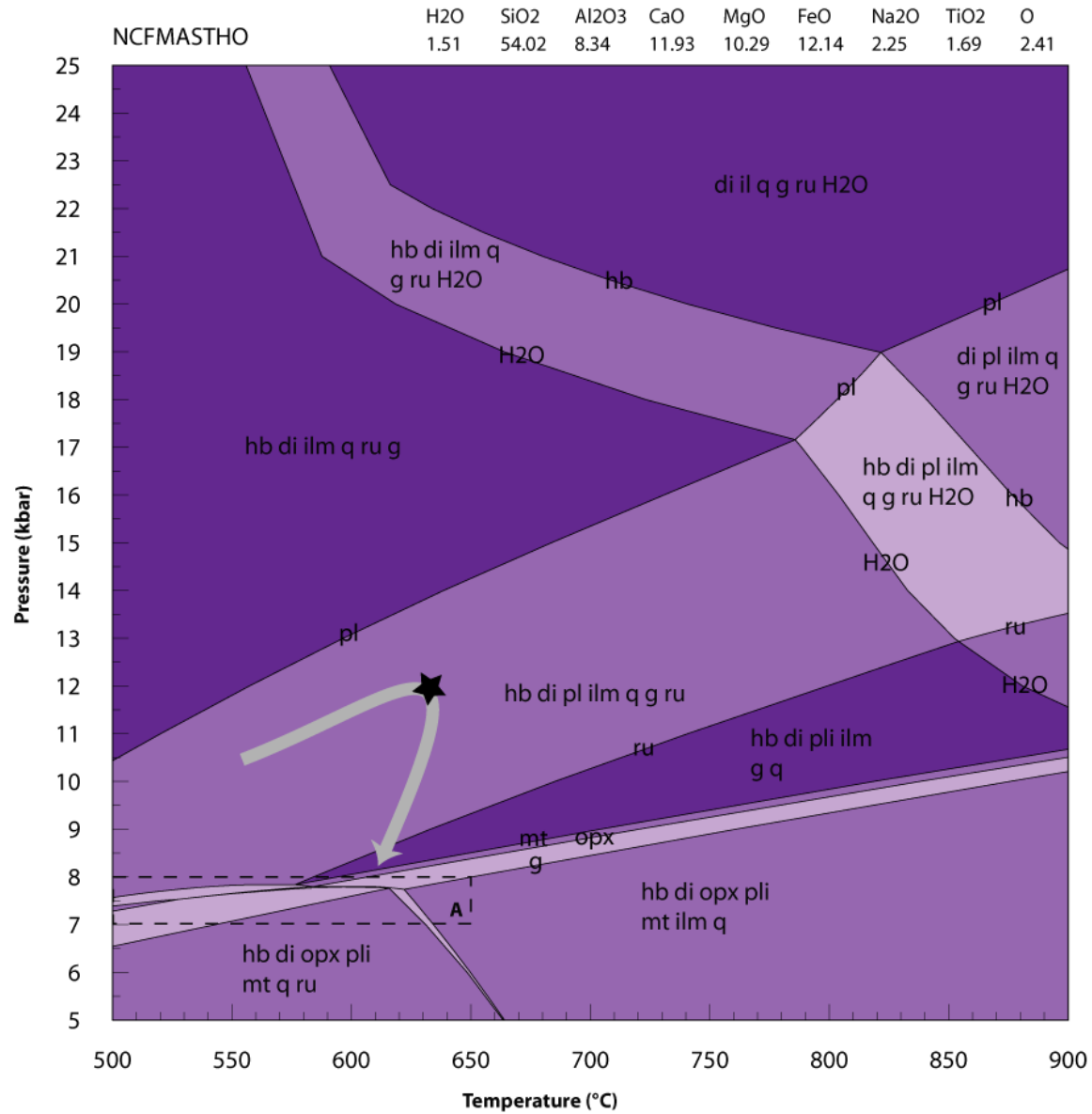
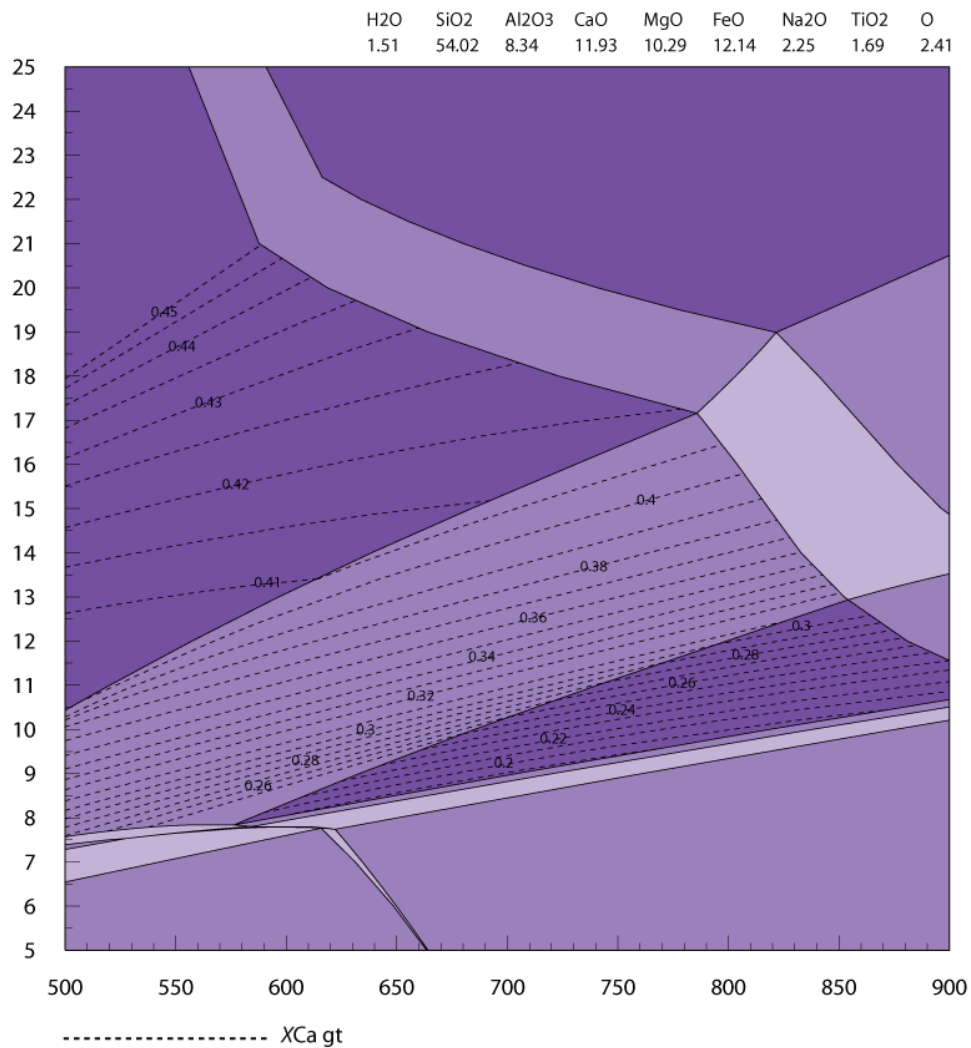


Figure 14

(b) Pseudosection A325-535A with compositional isopleths for XCa of gt



(c) Pseudosection A325-535A with compositional isopleths for XFe of gt

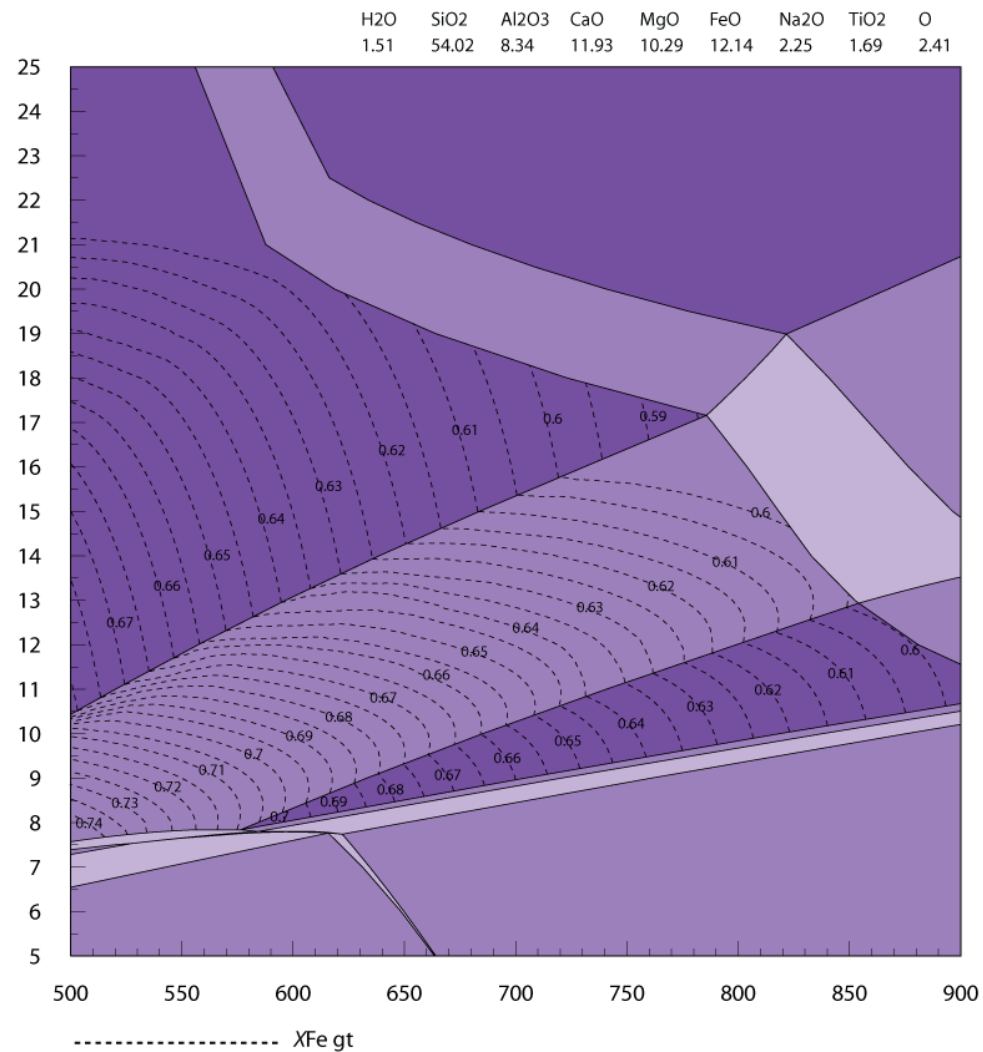


Figure 14

(c) Pseudosection A325-535A with compositional isopleths for XFe of cpx

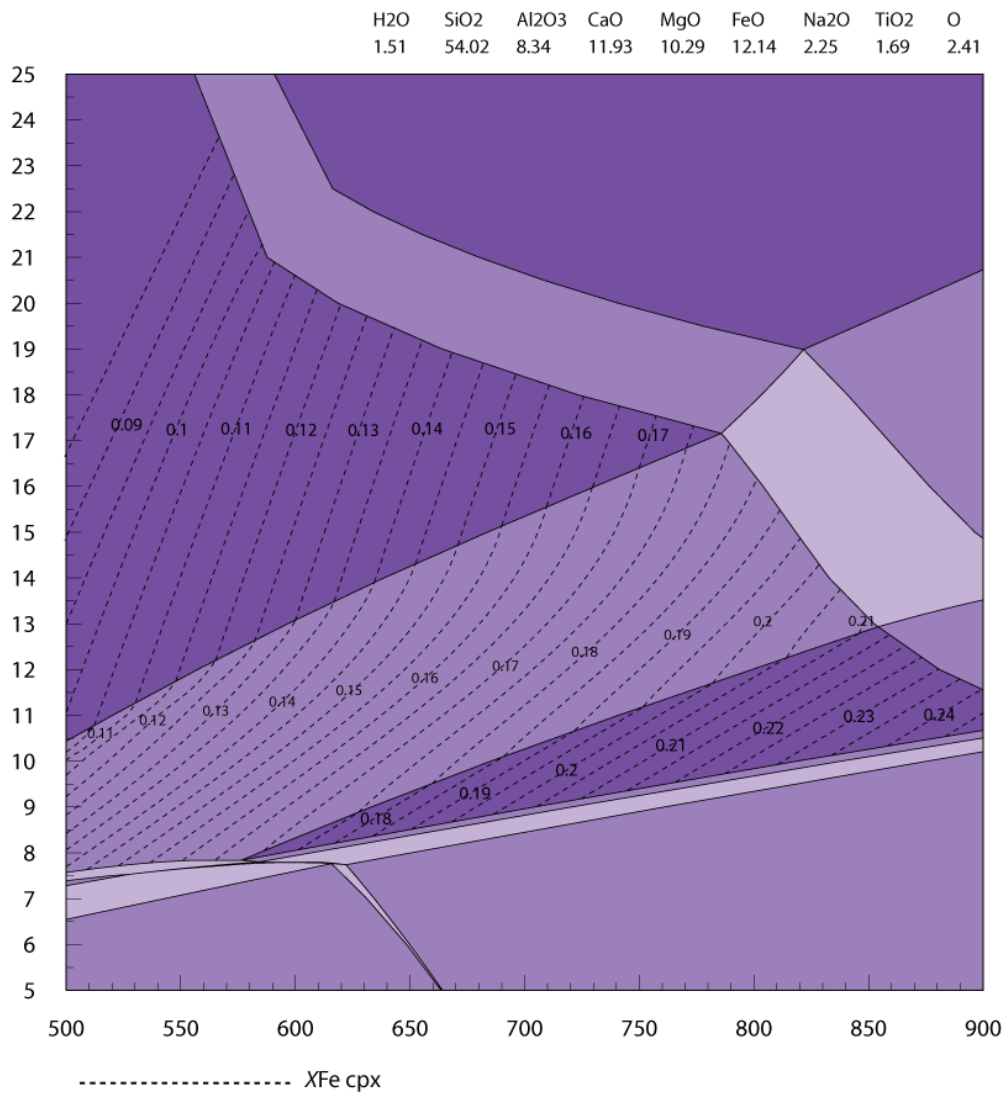


Figure 14

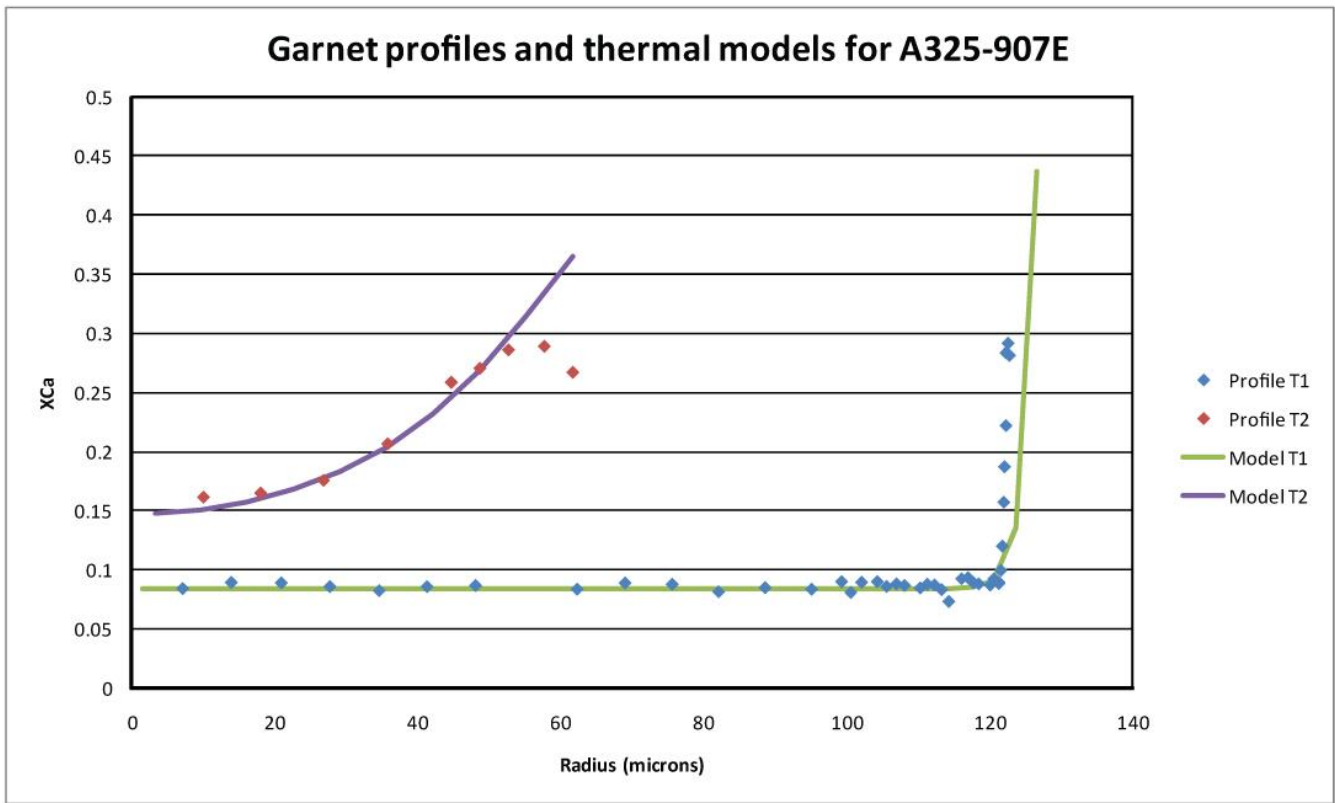
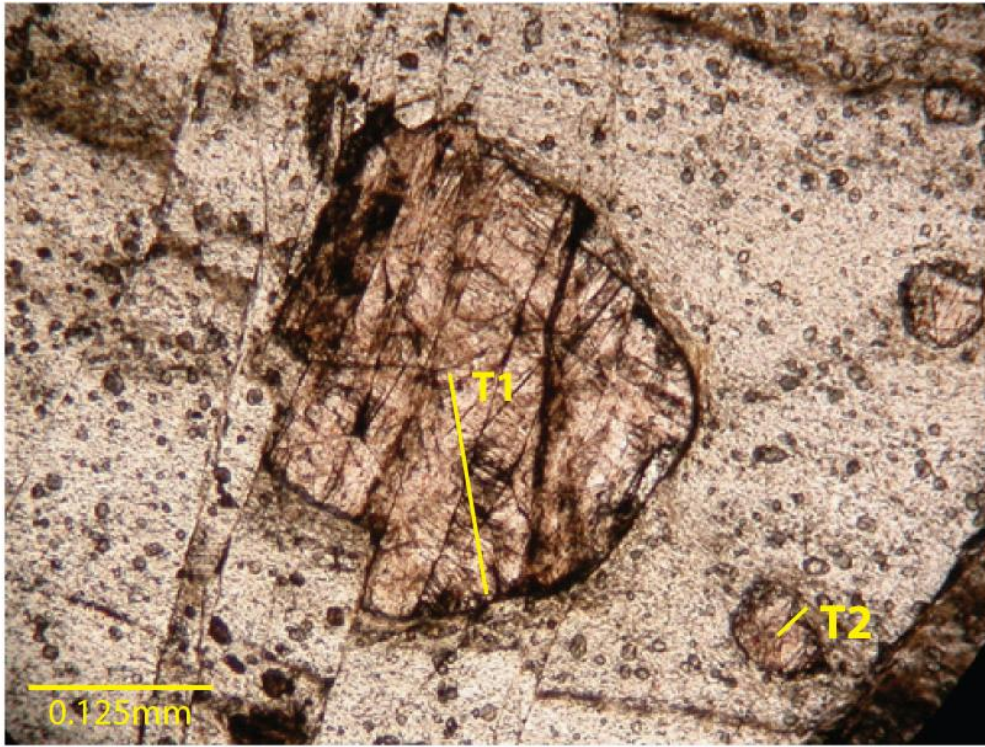


Figure 15

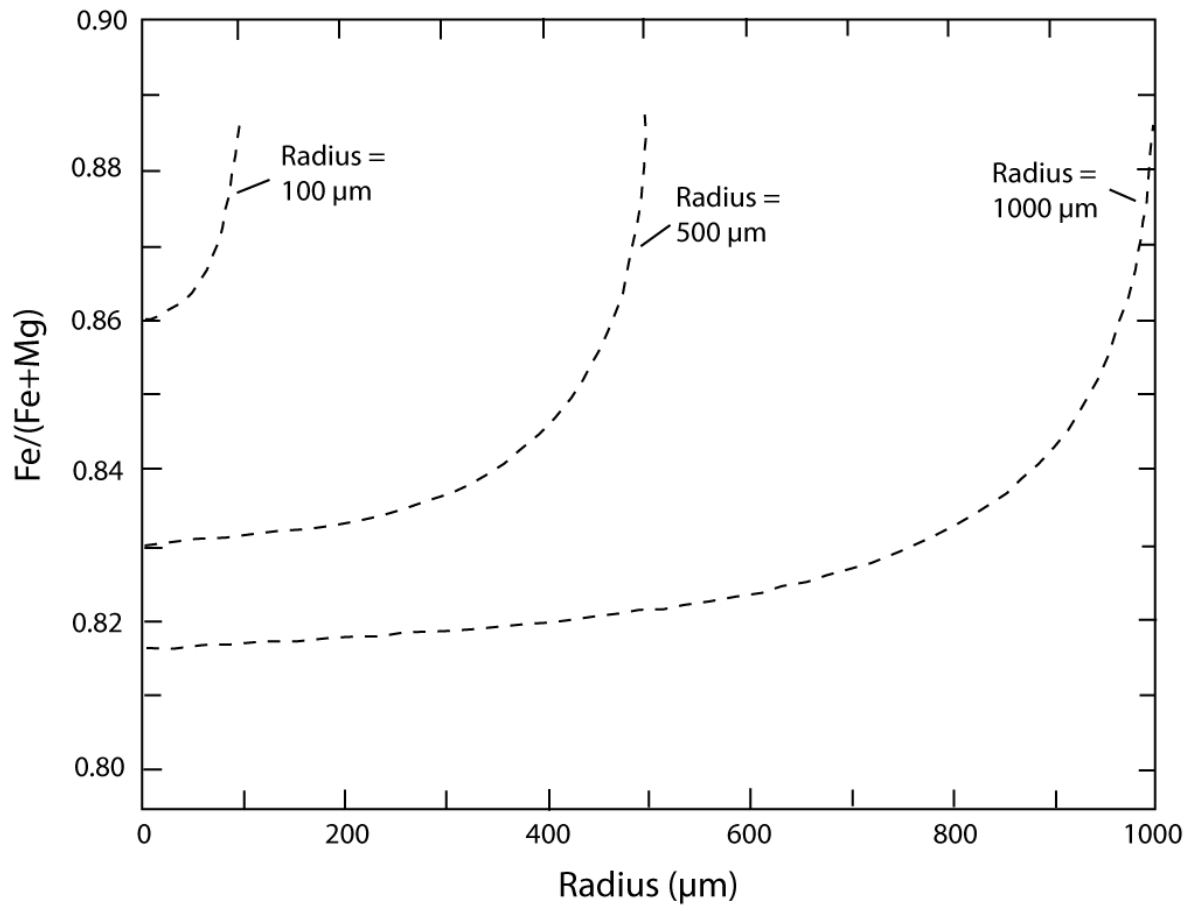


Figure 16